JFY2015

Japan Aerospace Exploration Agency

Commissioned Research Agreement

Algorithm Theoretical Basis Document

GCOM-C1/SGLI Snow/Ice Products

Upgrades, testing and validation (GCOM-C1 4^{th} RA 401)

JX-PSPC-419712

March 2016

Dr. Knut Stamnes (PI)

Stevens Institute of Technology

Contents

1 Introduction

1.1 Scope of the project

To create GCOM-C1/SGLI snow/ice products we have developed algorithms for cloud mask and surface classification, snow grain size retrieval, and surface temperature retrievals. These algorithms are based on the work we did for ADEOS-II/GLI (Stamnes et al., 2007; Aoki et al., 20017; Hori et al., 2007), but we used the new SGLI channels, upgraded the surface classification algorithm, and improved the accuracy of the retrieved snow grain size and aerosol properties as well as the surface temperature. These improvements have been accomplished by using a linearized radiative transfer model (RTM) for the coupled atmosphere-snow system in conjunction with a 2-layer snow model to allow for simultaneous retrieval of snow and aerosol properties, and by using the response functions of the SGLI IR channels and updated sounding data for the temperature retrieval. To test the performance of these algorithms and thereby obtain further improvement, we proposed to (i) upgrade the quality and accuracy of our cloud mask algorithm over snow/ice cover area, (ii) upgrade and test our surface classification algorithm over mixed snow/forest areas, (iii) develop and test algorithms for direct retrieval of snow/sea ice albedo, (iv) explore the potential for improved snow retrieval by assuming non-spherical snow grains, (v) use the direct albedo retrieval method to assess the quality of albedo estimates derived from inferred snow parameters, and (vi) explore the merits of using polarization channels to improve the aerosol retrieval to the extent available time and resources permit.

Figure 1 and Table 1 provide a summary of our products and the research schedule for each of our product, respectively.

1.2 Major objectives

The major objectives of our work are to:

1. Develop an improved cloud mask algorithm over snow/ice covered areas that is optimized for high latitude and high surface elevation areas.

2. Develop an improved surface classification algorithm with improved snow/sea ice, snow/forest classification.

3. Develop and test algorithms for direct retrieval of snow/sea ice albedo.

4. Explore the potential for improved snow retrieval by assuming non-spherical snow grains.

5. Use the direct albedo retrieval method to assess the quality of albedo estimates derived from infrared snow parameters.

6. Explore the merits of using polarization channels to improve the aerosol retrieval to the extent available time and resources permit.

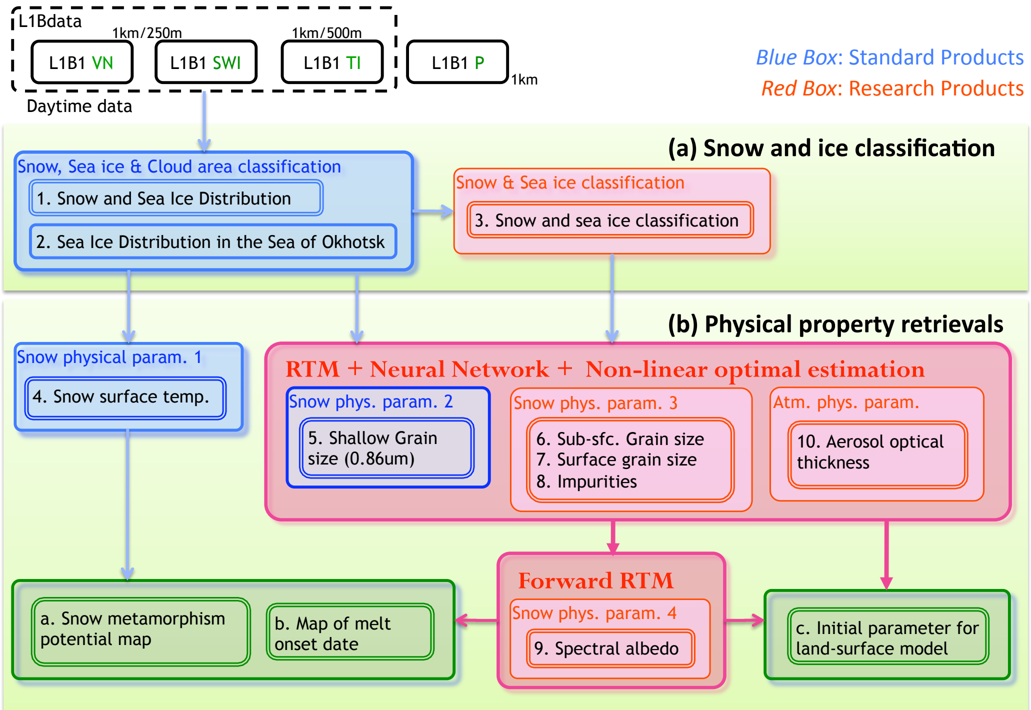

Figure 1: Schematic illustration of our products and the flow of the retrieval process. Blue and red boxes are the standard and research products, respectively.

1.3 Main goals and our work in JPY2015

The main goals and our work in JPY2015 can be summarized as follows:

- To test and validate our new C1 cloud mask algorithm for snow covered land areas; (see Section 2.1.2);
- To test and improve the C1 surface classification algorithm over Arctic ocean for sea-ice area by using MODIS images (see Section 2.1.3);
- To test and validate the implementation of C1 cloud mask algorithm to SGLI sensor (see Section 2.1.5);
- To implement Voronoi particle snow model into the SGLI snow retrieval code (see Section 2.2.1 about snow model and its phase function);
- To compare the retrieved snow grain size from both spherical and non-spherical particle snow models using MODIS data (see Section 3.2.2);
- To update snow/ice surface temperature retrieval based on the new SGLI channels response function (see Section 2.3).

- To explore the potential of using SGLI polarization channels to improve aerosol retrieval over snow (See Section 2.4).

The research schedule for these tasks are listed in Table 1.

Table 1: Our products for snow and ice classification shown in Fig. 1.

No.	item	Research Schedule
1	Upgrade cloud mask over snow/ice covered areas	Aug. 2013 - Mar. 2014
2	Upgrade surface classification	Aug. 2014 - Mar. 2015
3	Develop sea ice surface direct albedo	Apr. 2014 - Mar. 2015
4	Use direct albedo to assess the quality of snow parameters retrieval	Aug. 2013 - Mar. 2016
5	Explore non-spherical snow grains retrieval	Apr. 2014 - Mar. 2016
6	Explore SGLI polarization channels to improve the aerosol retrieval	Apr. 2014 - Mar. 2016

1.4 Overview of our work from JPY2013 to JPY2015

In this 3-year project, we upgraded and validated our cloud mark algorithm and surface classification algorithm; developed a sea-ice surface direct albedo algorithm; improved the snow grain size retrieval algorithm by using a non-spherical Voronoi particle model instead of the spherical particle model; and explored the potential for improving the aerosol retrieval by using SGLI polarization channels. An overview of the completed tasks are as follows:

- Upgrade of the cloud mask over snow/ice area. A new set of tables with dynamic thresholds was established to improve the quality of the cloud detection. It includes the consideration of solar/viewing geometry, atmospheric vertical structure, and surface elevation. This new algorithm has be applied to MODIS data, and validated by comparison with CALIPSO overpasses. Although SGLI has fewer thermal channels than MODIS, the new algorithm performs better than the MODIS MYD35 product [Chen et al., 2014].

- Upgrade of the cloud mask over land, desert, and snow mixed with vegetation areas. Based on the CALIPSO and MODIS products, we generate a neural network table to improve the quality of the cloud mask over such areas. This unique method is expected to imrpove the cloud mask, specially in the winter season and over desert areas. Comparisons with MODIS and CALIPSO show a significant improvement over our previous algorithm. The performance in the winter season is much better than that of the MODIS products.

- The sea-ice coverage detection has been updated too, but further validation is needed. We are searching for measurements that can be used for this propose.

- A sea-ice model has been implemented in our radiative transfer model. Based on it, we developed a new algorithm to retrieve the direct sea-ice surface albedo. This product is similar to our direct snow albedo algorithm. The albedo will be directly retrieved from the satellite radiances. Applications to real data retrieval and validation will be needed in the future.

- Comparisons between snow direct albedo and indirect albedo, can be used to assess the quality of retrieved snow parameters. Since the quality of the cloud mask and the surface classification has been greatly improved, we now find the direct and indirect albedo values to be very close. This method can remove pixels with large bias in the snow retrieval.

- In order to verify the snow model used in snow grain size retrieval, we compared the modeled snow BRDF with measurements obtained by the NASA Cloud Absorption Radiometer (CAR) deployed by aircraft over Elson Lagoon, Barrow, Alaska, on April 7, 2008. These comparisons show that non-spherical Voronoi particles provides better agreement between modeled and measured snow BRD than a spheric particle model. The current Voronoi particle model still leaves room for improvement, which will be pursued in our work over the next three years. The new non-spherical Voronoi particle snow model has been implemented into the snow grain size retrieval code. Preliminary result are presented in this report.

- We did a first sensitivity study using the polarization channels. The results show that the polarized reflectance provides an opportunity to distinguish aerosol optical thickness from snow impurity. The design of the SGLI polarized sensor helps make this distinction possible, because the scattering angles are in the forward direction.

We have completed the 3-year RA4 project. The cloud mask algorithm C1 and the snow retrieval algorithm C2 have been greatly improved and validated. For the next 3 years of the RA6 project, we will focus on further validation of these two algorithms using MODIS data and the new SGLI data. Also, we will improve the non-spherical particle snow model and continue exploring the merit of using SGLI polarization channels and multiple-angle measurements to improve aerosol retrievals over snow.

2 Theoretical Description of the Algorithms

2.1 C1: Cloud mask and surface classification

2.1.1 Identifying snow/ice fields: the NDSI test

The processing flow of the C1 algorithm starts with a Normalized Difference Snow Index (NDSI) test. The NDSI method has a long history and has been extensively utilized for cloud screening and detection of snow/ice covered areas [Hall et al., 1995, 1996, 2001]. The NDSI is defined as a normalized difference between the reflectance in two bands:

$$\text{NDSI} \;=\; \frac{R_{\text{VIS}} - R_{\text{SWIR}}}{R_{\text{VIS}} + R_{\text{SWIR}}} \tag{1}$$

where R_{VIS} is the observed reflectance of a channel in the visible spectral range and R_{SWIR} is the observed reflectance of a channel in the shortwave infrared spectral range. For the

MODIS instrument R_{VIS} is selected to be band 4 (0.55 μm) and R_{SWIR} to be band 6 (1.64 μm, Terra) or band 7 (2.13 μm, Aqua). By choosing an appropriate threshold (NDSI $\geq$ 0.4 as proposed by Hall et al. [1995]), the NDSI method can effectively identify snow/ice covered areas from other surface types as shown by Ackerman et al. [1998] and Salomonson & Appel [2004, 2006]. It can also be used to separate clouds (especially water clouds) from snow/ice surfaces. In the C1 algorithm we apply the the NDSI method of Hall et al. [2001] because we have found it to be very effective in identifying possible snow/ice covered areas including partially snow-covered areas (snow mixed with vegetation). However, we have also found, as discussed by Hutchison et al. [2013], that the NDSI method alone cannot completely separate clouds from snow, because some clouds, especially thin ice clouds and overlapping ice and water clouds, have NDSI signatures very similar to those of snow and ice. Therefore, in our C1 algorithm the NDSI method is used as a first step to identify possible snow/ice covered areas for which more detailed cloud mask procedures must be applied for correct cloud identification. A flowchart of the algorithm is provided in Figure 2.

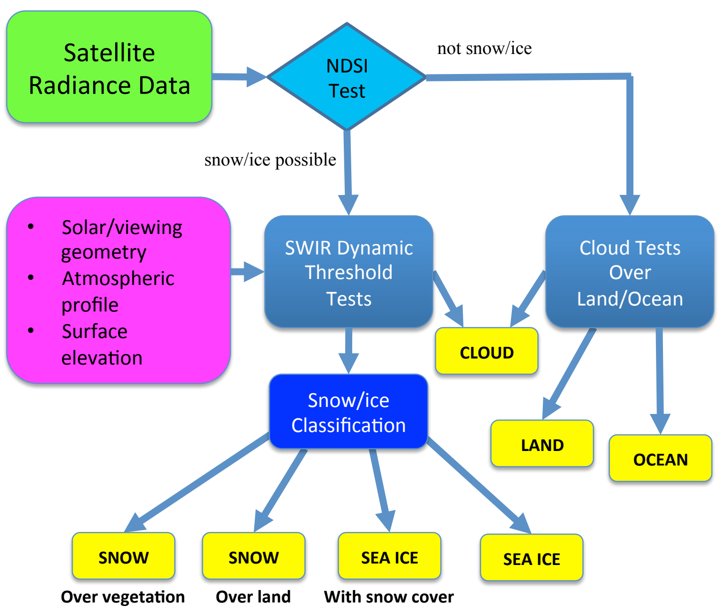

Figure 2: Flow chart of the C1 cloud mask algorithm over snow/ice surfaces.

2.1.2 Cloud tests over snow-covered land

The use of SWIR tests to separate clouds from snow has been discussed in some detail by Miller & Lee [2005], who used a combination of VIS, SWIR and 1.38 μm thresholds with a simple solar zenith angle correction. Trepte et al. [2002] used the MODIS 1.64 μm reflectance as well as the reflectance ratio between the 1.64 μm and the 0.65 μm channels to distinguish clouds from snow in polar regions. We tried to use a single SWIR threshold (2.13 μm) first to distinguish clouds from snow surfaces and found that most liquid water clouds and thick ice clouds have high 2.13 μm reflectance ($R_{2.13}$) because of their small particle size or high location in the atmosphere, which makes thresholding possible. However, we also found that a fixed threshold of $R_{2.13}$ is not appropriate because of the anisotropy of snow reflectance in the 2.13 μm channel. At low solar illumination angles (*i.e.* solar zenith angles $\geq 70°$) the threshold value should be higher than at nadir to avoid mis-classification of snow as clouds. Furthermore, we found seasonal and surface elevation dependence of the threshold value mainly due to different atmospheric absorption (primarily water vapor absorption) of the reflected 2.13 μm signal under different surface elevation and atmospheric conditions. For example in Greenland, snow surfaces generally look "brighter" in Spring than in Summer and Autumn, implying that higher thresholds must be applied. Also, we should use a higher threshold value at Automated Weather Station (AWS) Summit (elevation: 3,254 m) than at Swiss camp (elevation: 1,149 m) since the snow surface at Summit would generally have higher 2.13 μm reflectance than the same snow surface at Swiss camp under the same solar/viewing geometry. In order to accommodate these many factors, we use the following strategy: The threshold is set to be the 'maximum possible snow reflectance' defined as the simulated $R_{2.13}$ reflectance of 'very fine grained' snow for a given elevation and atmospheric condition. We chose to model reflectance of snow instead of clouds for the cloud mask development because there could be many types of clouds over snow making it difficult to decide what kind of $R_{2.13}$ reflectance a cloud should have. However, if we can establish "the maximum $R_{2.13}$ value that a natural snow surface can have" then the situation becomes more clear. We finally chose $R_{2.13}$ reflectance of snow with effective grain size $r_{\mathrm{eff}} \approx 25\,\mu$m as the threshold ($\mathrm{Th}_{R_{2.13}}$) since this grain size is smaller than most of the snow grains that exist in nature. By applying this threshold, water clouds and thick ice clouds with high 2.13 μm reflectance can be distinguished without mis-classifying most snow pixels as clouds. Lookup tables that cover all possible solar/viewing geometries applicable for daytime operation of the SGLI were prepared so that for each satellite pixel an appropriate threshold value can be dynamically determined consistent with the actual solar/viewing geometry.

We further explored the dynamic threshold method by using two SWIR channels (*i.e.* MODIS channels at 1.64 μm and 2.13 μm for Terra, and at 1.24 μm and 2.13 μm for Aqua). Figure 3 is a radiative transfer simulation of MODIS channel 6 (1.64 μm) and channel 7 (2.13 μm) reflectances of water/ice and mixed phase clouds over snow surfaces with different snow grain sizes under a common solar/viewing geometry (solar zenith angle (SZA) = 60°, viewing zenith angle (VZA) = 20°, relative azimuth angle (RAZ) = 112°) in the polar regions. In the simulations we used the Sub-Arctic Summer atmospheric profile; the snow surfaces are assumed to consist of snow with effective grain sizes of 50, 100 and 400 μm; a liquid water cloud, located at 2 km above the snow surface, assumed to have an effective particle size of 15 μm; an ice cloud, located at 10 km altitude, assumed to have an effective particle size of 42 μm. The inherent optical properties (IOPs) for water clouds were obtained from the parameterization of Hu & Stamnes [1993] and ice cloud IOPs were taken to be that of "rough aggregate" particles in the parameterization by Key et al. [2002]. The optical depth for water/ice clouds at 0.645 μm ranged between 0.01 and 5. Additional calculations of the snow cases (grain radius range: 15 - 2000 μm) in the absence of clouds were also performed. All the calculations were performed using an extended version of the DISORT [Stamnes et al., 1988a] radiative transfer model with a Earth curvature correction [Dahlback & Stamnes, 1991]. In Fig. 3 reflectances of clouds over snow cases are represented by colored symbols: green for ice clouds, cyan for water clouds and blue for mixed ice and water clouds. Different symbols indicate different cloud optical depths. For example, the three green 'crosses' represent the reflectance of ice clouds with optical depth $\tau_i = 0.1$ over snow with $r_{\mathrm{eff}} = 400$, 100, and 50 μm, while the green 'circles' are for $\tau_i = 0.5$ cases. Green dashed lines indicate ice cloud cases with different optical depths over an underlying snow surface with the same grain size. Reflectances of snow in the absence of cloud cover are represented by the black dots.

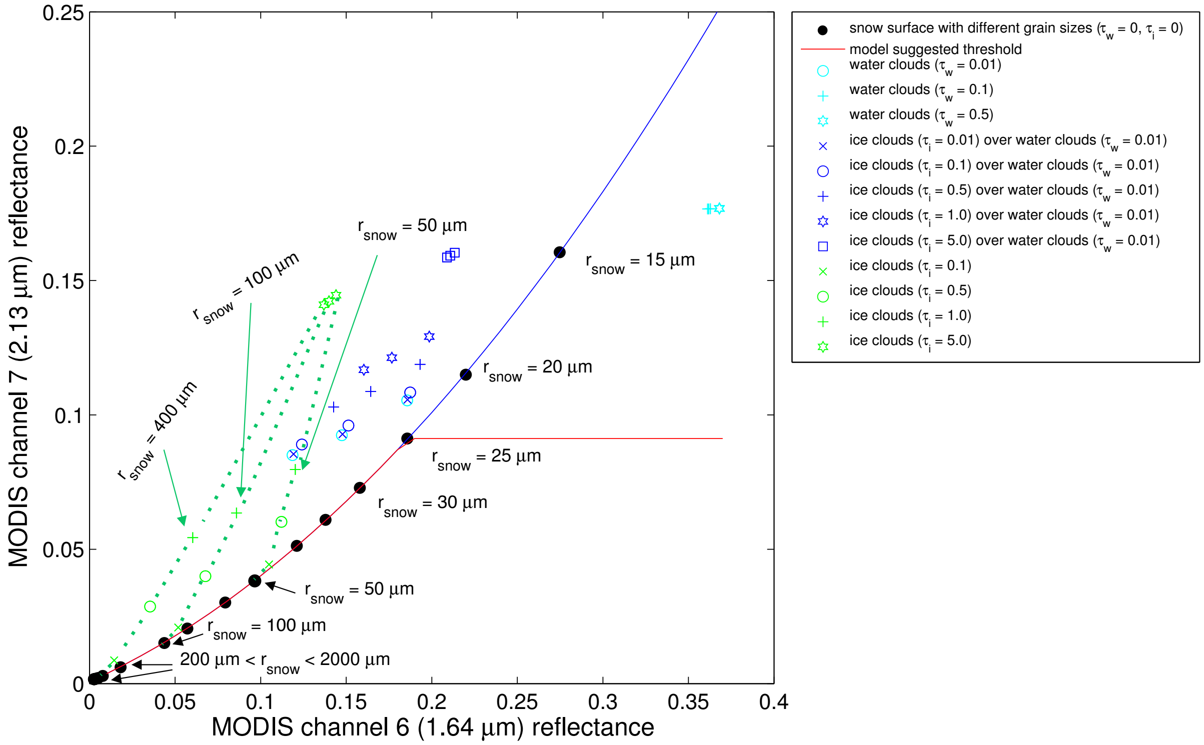

Figure 3: Simulated $R_{2.13}$ and $R_{1.64}$ of clouds over snow. r_{snow} is the effective grain radius of the snow; three 'background' snow grain radii (50, 100 and 400 μm) are used when simulating the reflectances of cloud over snow, τ_w and τ_i are water and ice cloud optical depth at 0.645 μm respectively. Sub-Arctic Summer atmospheric profile is used in the simulation and the solar/viewing geometry adopted in this figure is: solar zenith angle (SZA) = 60°, viewing zenith angle (VZA) = 20°, relative azimuth angle (RAZ) = 112°.

From the simulated results we can infer:

- The reflectance from water clouds in the SWIR channels increases drastically as their optical depth increases and it saturates at a higher level than that of snow. More importantly, the reflectance from water clouds depends little on surface properties (except for the extremely thin ($\tau_i = 0.01$) cases), which might indicate that a constant $R_{2.13}$ or $R_{1.64}$ threshold would be good enough to separate water clouds from underlying snow surfaces.

- The reflectances of mixed ice and liquid water clouds are largely dominated by the contribution from water droplets (even with optical depth 0.01) implying that they might also be distinguished from snow in a way similar to that for water clouds.

- For ice clouds the situation is more complicated. We can see that very thin ice clouds (like the green 'crosses' with $\tau_i = 0.1$) are very difficult to distinguish from snow since their reflectances closely resemble those of snow with smaller grain sizes. We also find that the reflectance for thin to moderately thick ice clouds ($\tau_i = 0.1 \rightarrow 1$) depends strongly on the reflectance contribution of the snow surfaces underneath. The green 'circles' in Figure 3 show that ice clouds with $\tau \approx 0.5$ or thinner might be separated from the cloud free cases by a proper thresholding method.

An illustration of the 'Model Suggested Threshold' (MST) for the particular solar/viewing geometry adopted in Fig. 3 is shown as the red line. The threshold consists of two parts: the horizontal part is the aforementioned $R_{2.13}$ threshold ($\mathrm{Th}_{R_{2.13}}$), which is calculated from the reflectance of 'very fine grained' snow ($r_{\mathrm{eff}} \approx 25\,\mu$m) and is designed to pick up thick ice clouds and liquid water clouds. The curved part (blue line) is a quadratic fit to the 1.64 μm and 2.13 μm reflectances of snow, designed to pick up thinner ice clouds. For a possible snow pixel it is calculated as $\mathrm{Th}_{R_{2.13} \succ 1.64} = c_0 + c_1 R_{1.64} + c_2 R_{1.64}^2$, where $R_{1.64}$ is the 1.64 μm reflectance of that pixel, the symbol $\succ$ indicates the dependence of this threshold on the $R_{1.64}$ reflectance. The fitting coefficients c_0, c_1 and c_2 depend on the solar/viewing geometry. Figure 3 shows that cloudy cases are 'above' the MST line in the $R_{1.64}$ - $R_{2.13}$ space which implies that a snow pixel with 2.13 μm reflectance greater than the corresponding MST value is suspected to be cloud contaminated. The 'clear confidence' indices are estimated linearly using the two parts of the MST ($\mathrm{Th}_{R_{2.13}}$ and $\mathrm{Th}_{R_{2.13} \succ 1.64}$ respectively), ranging between 0% clear ('confident cloudy') and 100% clear ('confident clear') and the final clear confidence level is taken to be the minimum value of the two calculated clear confidence indices. The thresholds and corresponding confidence levels are summarized in Table 2. An artificial offset f is added to the curved part of the threshold to accommodate errors from the model. Currently f is set to be 0.0016 for the test over the Greenland region. The simulation using the 1.24 μm and 2.13 μm channels of MODIS Aqua yielded similar results, except that a four degree polynomial was needed to fit the curved part of the suggested threshold. So the corresponding formula for the curved part of the threshold would become: $\mathrm{Th}_{R_{2.13} \succ 1.24} = c_0 + c_1 R_{1.24} + c_2 R_{1.24}^2 + c_3 R_{1.24}^3 + c_4 R_{1.24}^4$. A multi-linear interpolation scheme is used to dynamically interpolate the suggested threshold line according to the solar/viewing geometry of each satellite pixel. The threshold depends on season, location and surface elevation. Currently, three model atmospheric conditions: Sub-Arctic Summer, Sub-Arctic Winter and Mid-latitude Winter are tested and a model-based scaling method (please see Chen et al. [2014] for details) is applied to deal with potential issues associated with the surface elevation.

2.1.3 Cloud test over sea ice and ocean

The above SWIR dynamic threshold tests are all designed for snow covered land areas. Over ocean areas we use the ratio of $\mathrm{R}_{2.13}/\mathrm{R}_{0.65}$ instead of $\mathrm{R}_{2.13}$ since for some clouds over ocean

Table 2: SWIR test thresholds for clear confidence level determination

Threshold part	**Threshold value and clear confidence**	
	Confident clear	Confident cloudy
Horizontal Part	$R_{2.13} \leq \mathrm{Th}_{R_{2.13}}$	$R_{2.13} \geq \mathrm{Th}_{R_{2.13}} + 0.05$
Curved Part	$R_{2.13} \leq \mathrm{Th}_{R_{2.13 \succ 1.64}} + f$	$R_{2.13} \geq \mathrm{Th}_{R_{2.13 \succ 1.64}} + f + 0.05$

the 2.13 μm signal would be too low to pass the $R_{2.13}$ threshold, and hence the algorithm will mis-identify those cloudy pixels as sea ice pixels. However, the ratio $R_{2.13}/R_{0.65}$ would still be high enough to allow a proper thresholding method to be applied. Again, this threshold is dynamically calculated like in the $R_{2.13}$ method.

2.1.4 Surface classification approach

Another feature of the C1 algorithm is that it provides a detailed classification of the ice type and snow coverage over sea ice. As discussed by Stamnes et al. [2011], different ice types have very different ice albedo due to different amounts of scattering inclusions and ice impurity concentrations, and small amounts of snow on sea ice will significantly change the albedo of the ice. Thus, a detailed surface classification of sea ice is necessary to obtain a robust surface retrieval algorithm. We applied the Normalized Difference Ice Index (NDII) method to achieve this goal in our GLI products [Stamnes et al., 2007a]. Based on our experience with the GLI algorithm, we are developing a new surface classification algorithm in C1 using our comprehensive radiative transfer model for the coupled atmosphere-snow-ice-ocean system [Stamnes et al., 2011].

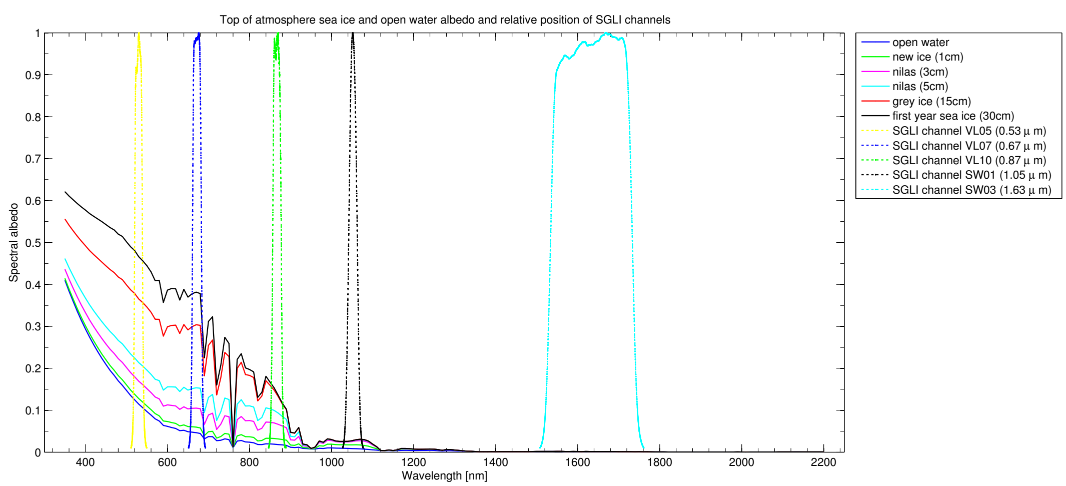

Figure 4: Simulated ice and open water spectral albedo and the relative position of SGLI channels.

Figure 4 shows the spectral albedo of different types of sea ice as well as open water. It can be seen that SGLI channel VL05 (0.53 μm) and VL07 (0.67 μm) are very sensitive to the thickness of sea ice and thus would be the optimum channels for sea ice classification and ice/open water separation. Another important task of the C1 algorithm is to separate snow-covered sea ice pixels from bare sea ice pixels since it is very important to provide correct pixel information to the C2 algorithm for sea ice/snow property retrieval. We simulated the spectral albedo of snow-covered and bare sea ice as shown in Fig. 5. It can be seen that snow and ice have very different albedo values in the NIR and SWIR regions, so SGLI channel VL10 (0.87 μm) and SW01 (1.05 μm) can provide valuable information to separate snow covered sea ice from bare sea ice. Due to the strong anisotropy of sea ice and snow reflectance in the NIR and SWIR region, dynamic thresholds that depend on solar/viewing geometry will be applied for this purpose.

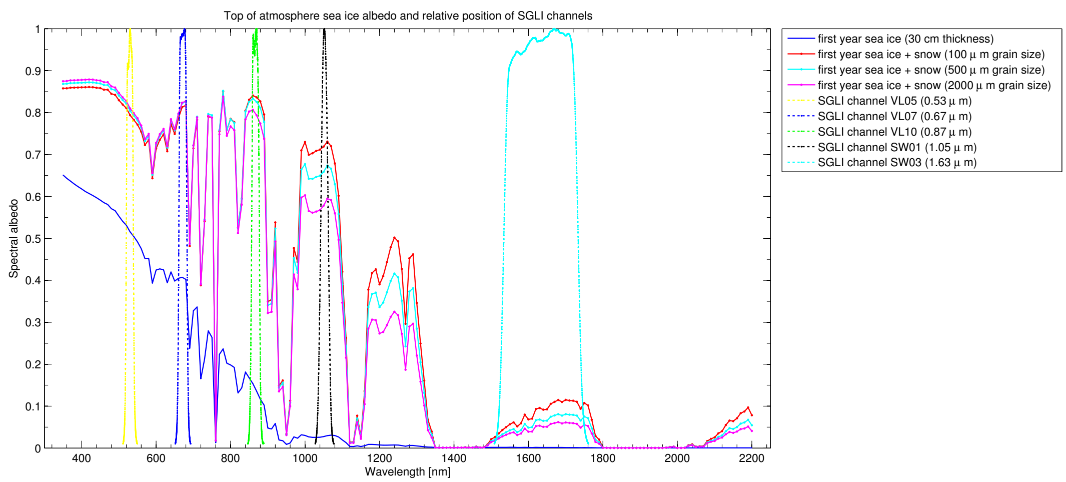

Figure 5: Simulated spectral albedo of snow covered/bare first year sea ice.

2.1.5 Adaptation of C1 algorithm to SGLI sensor

After our successful tests on MODIS data as described in Chen et al. [2014], we adapted our algorithm to use the channel specifications of GCOM-C1/SGLI and tested its performance using the SGLI test data. To distinguish clouds over snow covered area, we proposed to use SGLI channel SW03 (1.63 μm) and SW04 (2.20 μm) since they are the closest equivalents to MODIS channel 6 (1.64 μm) and channel 7 (2.13 μm). Following the same methodology as in our previous work, we simulated various cloud/cloud-free cases with different underlying snow conditions. The result, however, was very different from what we got for the MODIS channels. Figure 6 shows the simulation of pure ice clouds with different optical depths (green dots) over different snow cases (black dots) using MODIS (left) and SGLI (right) channel specifications. One can observe that the previously distinguishable cloudy/cloud-free cases under MODIS channel specifications are no longer distinguishable by SGLI as the cloudy and cloud-free cases are closely packed together. This result was unexpected since we thought, as described in Chen et al. [2014], that the combination of SGLI channel SW03 and SW04 should be an optimum choice for cloud screening over snow covered areas. We seriously investigated this issue in order to find the reason behind it since it can, if unresolved, render our SWIR cloud masking scheme inapplicable to the SGLI sensor.

We first noticed different profiles of gaseous absorption in MODIS and SGLI. Figure 7

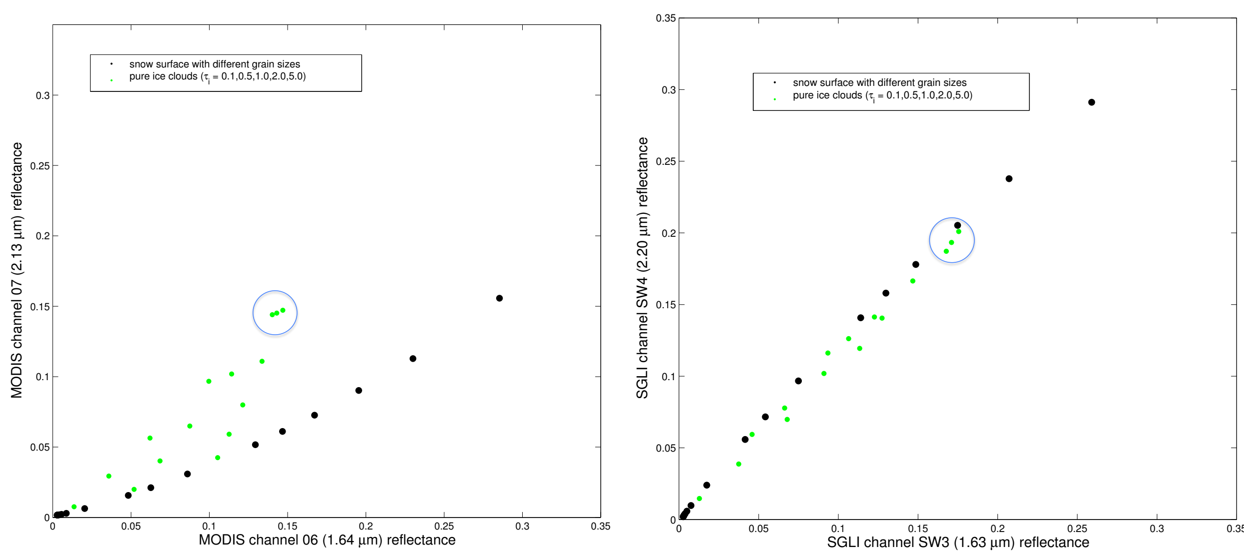

Figure 6: Simulated SWIR reflectance of snow (black dots) and ice clouds over snow (green dots). The ice cloud is assumed to be located at 10 km altitude with an effective particle size of 42 μm and a "background" snow effective grain sizes of 50, 100 and 400 μm. Cloud-free snow cases are assumed to have effective grain size between 15 to 2000 μm. Other settings of the simulation are identical to the simulation in our previous work [Chen et al., 2014]. **Left panel**: For MODIS sensor; **Right panel**: For SGLI sensor, note the cloudy cases (green dots) are no longer separable from snow cases (black dots) in the simulation for SGLI.

shows significant change in layer absorption optical depth between the two SWIR channels from MODIS to SGLI. However, as calculated that this change in gas absorption profile will only lead to a 4 to 7% difference in the simulation results, which will not be enough to explain the difference between the results for MODIS and SGLI as shown in Figure 6. So there must be some other reason for this difference. Next, we focused on the IOPs of clouds and snow that we used in the simulations. Figure 8 shows the single scattering albedo and asymmetry factor of snow particles in the SWIR spectral range. We can notice that:

- Snow particles have higher average single-scattering albedo in MODIS channel 6 ($1.64\mu m$) compared to that of MODIS channel 7 ($2.13\mu m$), which means that snow is more absorptive in MODIS channel 7 compared to MODIS channel 6. As the grain size becomes smaller (from $400\mu m$ to $100\mu m$) the difference in single-scattering albedo between MODIS channel 6 and channel 7 becomes larger. However, for the SGLI channels the differences in single-scattering albedo between two SWIR channels are much smaller compared to their MODIS counterparts.

- For the MODIS channels, the average asymmetry factor of snow particles is significantly higher in channel 7 than in channel 6. This difference implies that the phase function of snow will be more asymmetric in channel 7 (scatters more in the forward direction) compared to channel 6. For SGLI, however, the difference in asymmetry factor is also small between two SWIR channels.

The difference in snow IOPs suggests that we should look into the refractive index of ice in SWIR region. Figure 9 shows the refractive index of ice in the 0.9 to 2.4 μm wavelength range. One can see that while the real part of refractive index decreases smoothly from about 1.3 to 1.25, the imaginary part, which represents the absorption property of ice, has a peak at around 2μm. The close position of MODIS channel 7 to this peak results in significantly more absorption by ice particles in this channel compared to all the other SWIR channels in MODIS and SGLI (MODIS channels 5, 6, SGLI channels SW01, SW03 and SW04), which explains the difference of snow IOPs we found earlier. Moreover, since cloud particles (only ice cloud is discussed here since they are hard to detect compared to water clouds) are generally smaller than snow particles, the difference in IOPs between an "absorptive" channel (like MODIS channel 7) and a "non-absorptive" channel (like MODIS channel 6 or SGLI channel SW03) will be more significant. Figure 10 shows plots of the single-scattering albedo in the two sensor's SWIR channels with green colored symbols indicating those for MODIS (channel 6 and 7) and blue colored symbols those for SGLI (channel SW03 and SW04). It can be seen that for the MODIS channels the symbols indicating cloud particles are distinct from the line for snow particles with different grain sizes whereas this behavior is not true for SGLI. Hence the single-scattering albedo of ice cloud particles in the two SWIR channels resemble those of snow particles with small grain size for SGLI, which explains the simulation results for the SGLI sensor (Fig. 6 right panel) where the reflected signals from ice clouds are converging to the line indicating cloud-free snow cases as the cloud optical depth increases from 0.1 to 5.
Knowing that the difference in ice absorption is the main reason that we see different results in our simulations, we now try to follow the strategy of selecting one "absorptive" channel

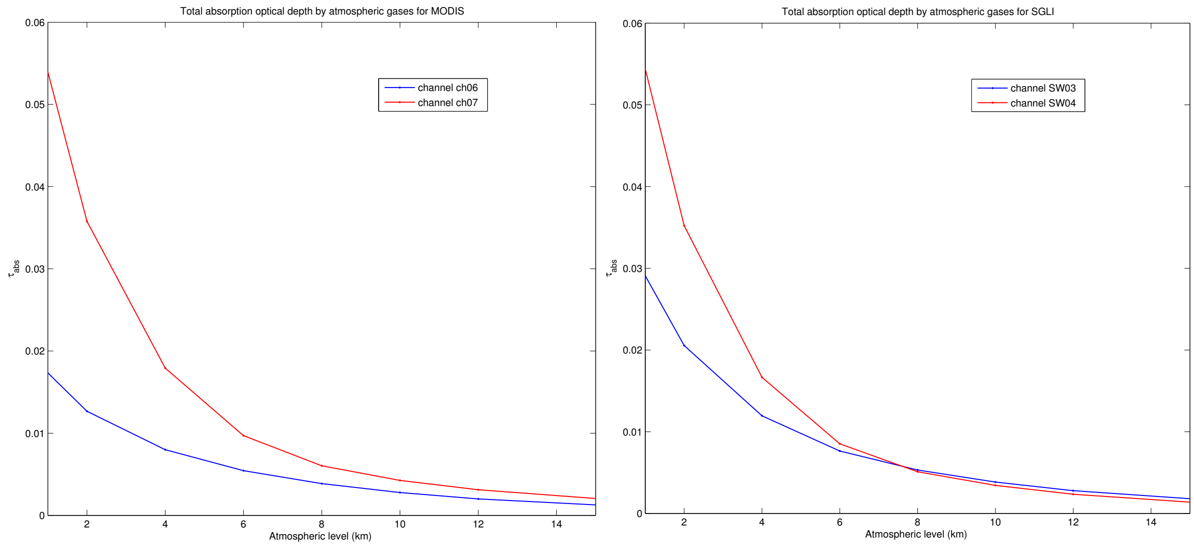

Figure 7: Gaseous absorption profile comparison between two SWIR channels. **Left**: MODIS channel 6 and 7; **Right**: SGLI channel SW03 and SW04

and one "non-absorptive" channel from SGLI for the cloud masking over snow. As shown in Fig. 9, ice is non-absorbing in SGLI channel SW01 and "slightly" absorbing in SGLI channel SW03 and SW04. So we followed our strategy to select two pairs of SWIR channels as SW01+SW03 and SW01+SW04 and did simulation accordingly. The results are consistent with our expectation as shown in Fig. 11, which demonstrates that cloudy and cloud-free cases are distinguishable. We actually used a similar channel choice in Chen et al. [2014], where MODIS channels 5 and 7 were used with Aqua MODIS data, and its performance was validated by collocated CALIOP measurements.

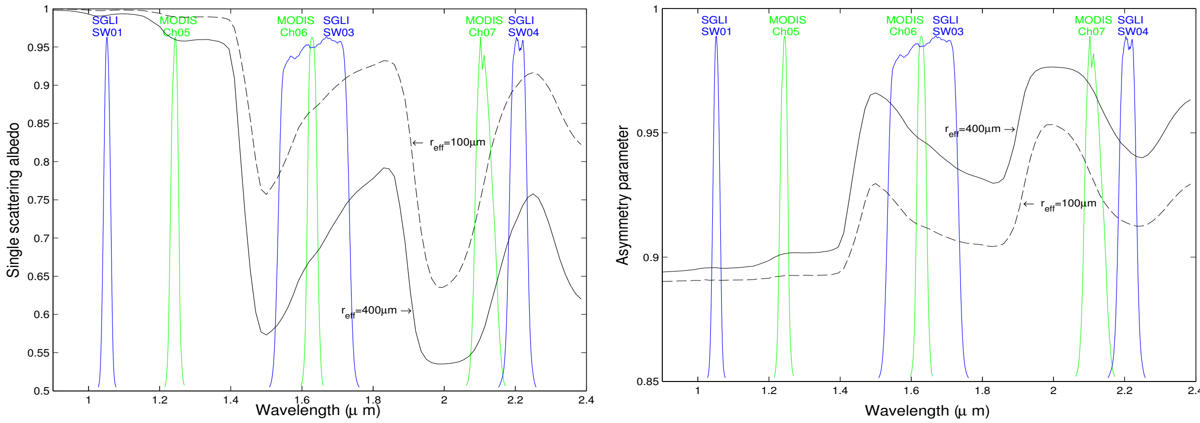

Figure 8: Inherent optical properties of snow particles (grain size 100 μm and 400 μm) in the SWIR region. **Left**: Single-scattering albedo; **Right**: Asymmetry parameter.

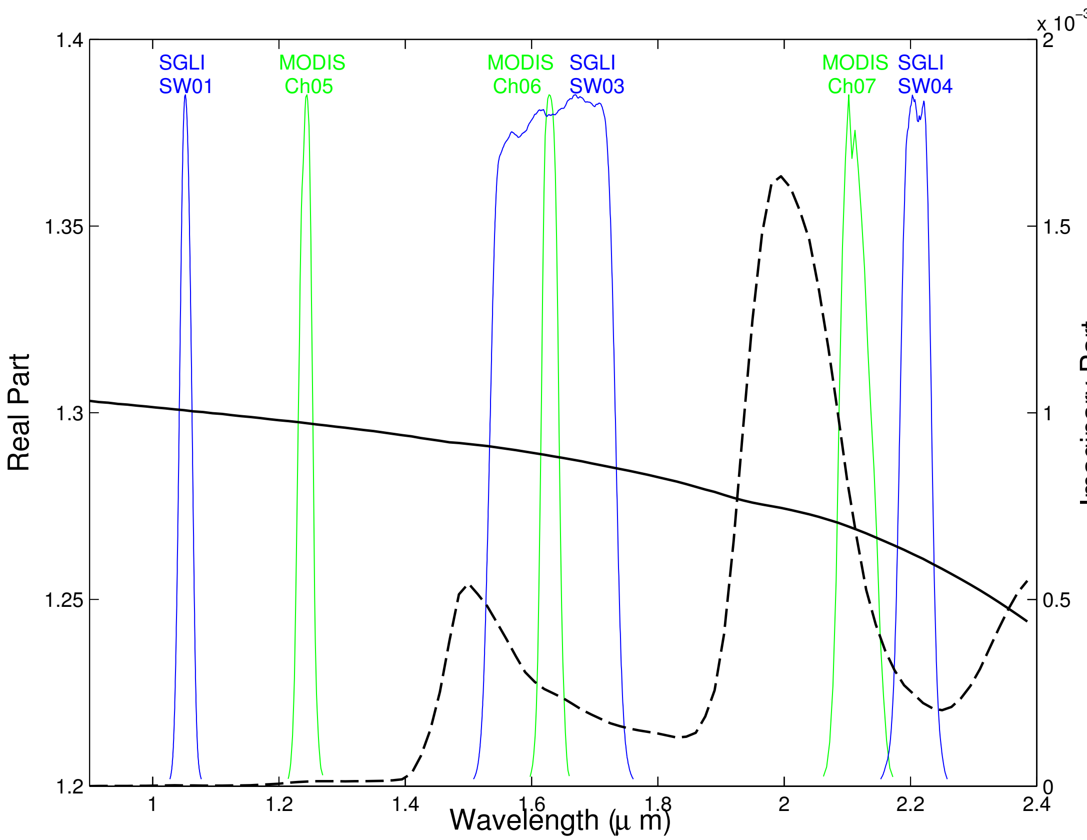

Figure 9: Refractive index of ice in the SWIR region. **Solid line**: real part; **Broken line**: imaginary part.

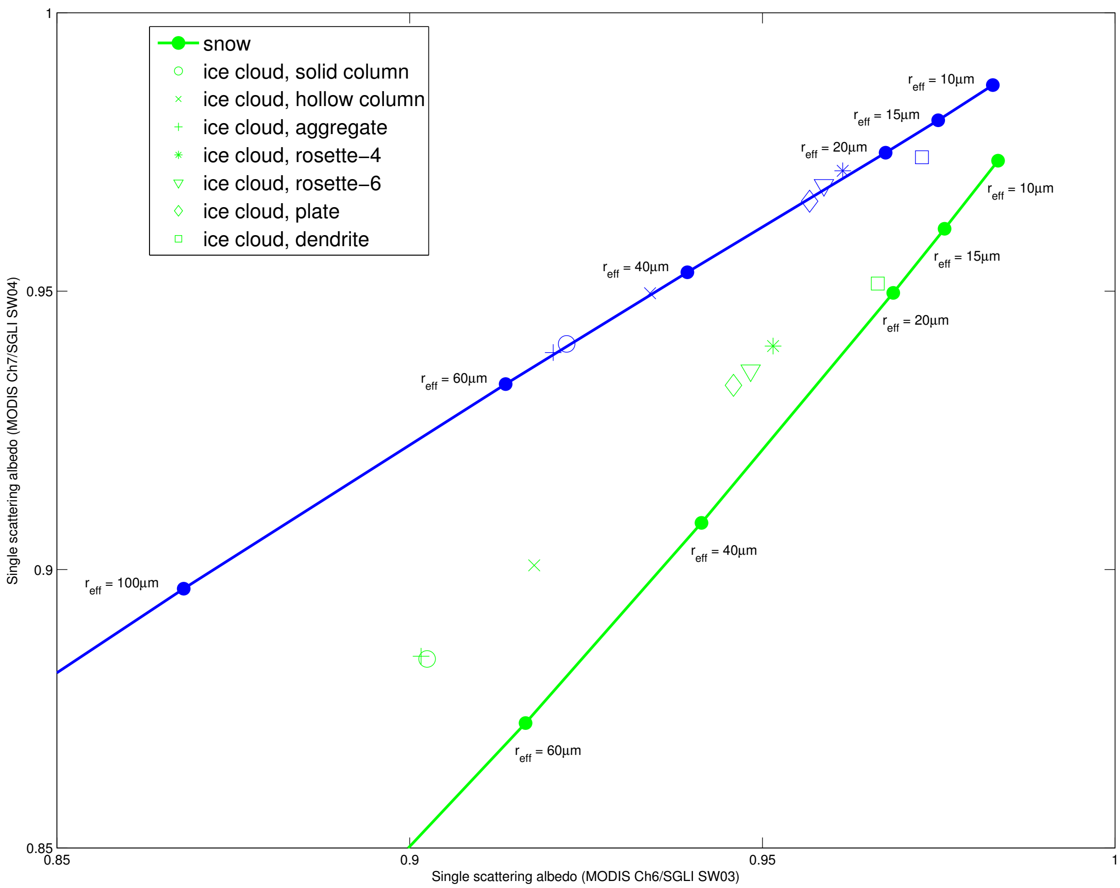

Figure 10: Single-scattering albedo of snow and ice cloud particles in the two SWIR channels. Results for MODIS channels 6 and 7 are shown in green and for SGLI channels SW03 and SW04 in blue.

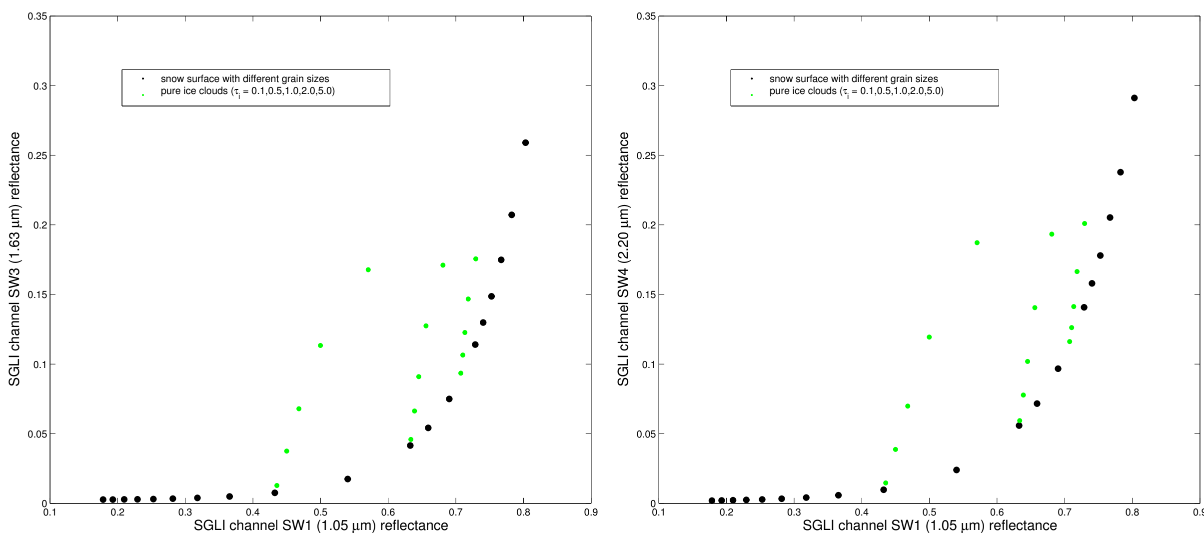

Figure 11: The same as Figure 6 but for alternative SGLI channels. **Left**: SGLI SW01 and SW03; **Right**: SGLI SW01 and SW04.

2.2 C2: snow, sea ice and atmospheric parameter retrievals

Basically three key steps are used to retrieve the snow and atmospheric parameters, (i) a forward radiative transfer model, (ii) a neural network training algorithm and (iii) a nonlinear optimal estimation method. Figure 12 shows a flow chart of the retrieval algorithm for snow and atmospheric parameters.

2.2.1 Forward radiative transfer model

The discrete-ordinate radiative transfer (DISORT) model for the atmosphere-snow system was used to calculate the radiance at the top of the atmosphere as a function of atmospheric and snow physical parameters [Stamnes et al., 1988b, 2007b]. This model has a pseudo-spherical treatment for solar beam attenuation in a curved spherical-shell atmosphere [Spurr, 2002], and it has been validated against Monte-Carlo results [Gjerstad et al., 2003]. We calculate the extinction coefficient, single-scattering albedo, and phase function using a Mie code based on conventional light-scattering theory, under the assumption of spherical grain shapes.

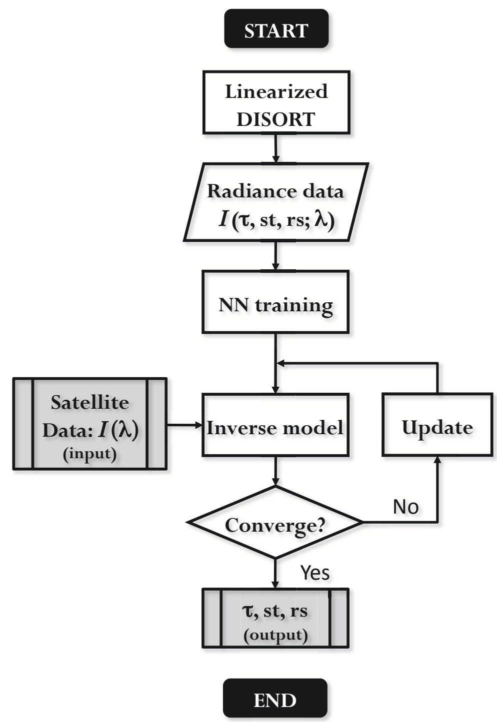

Figure 12: Flow chart of the atmospheric and snow parameter retrieval algorithm. All notations are described in the text.

Snow model In the snow model, since we know the size distribution of snow particles [Aoki et al., 2000], an effective snow grain radius is considered for the optical properties of snow. The size distribution of snow particles is a log-normal size distribution with a geometric standard deviation of 1.6 measured by Grenfell & Warren [1999a] in Antarctica. The refractive indices of ice are taken from the data compiled by Warren & Brandt [2008] (Fig. 13). For a mixture of snow/ice and impurities, the effective optical properties of the mixture are obtained by weighting each component so that the volume extinction coefficient $\tilde{\beta}_{\rm ext}$, the single scattering albedo ω and the phase function asymmetry factor g of an external mixture are obtained as follows:

$$\tilde{\beta}_{\rm ext} = (1-f)\tilde{\beta}^{ice}_{\rm ext} + f\tilde{\beta}^{imp}_{\rm ext} = [(1-f)\rho_s\kappa^{ice}_{\rm ext} + f\rho_{imp}\kappa^{imp}_{\rm ext}], \quad (2)$$

$$\omega = \frac{(1-f)\omega^{ice}\kappa^{ice}_{\rm ext} + f\omega^{imp}\kappa^{imp}_{\rm ext}}{(1-f)k^{ice}_{\rm ext} + fk^{imp}_{\rm ext}}, \quad (3)$$

$$g = \frac{(1-f)\omega^{ice}\kappa^{ice}_{\rm ext}g^{ice} + f\omega^{imp}\kappa^{imp}_{\rm ext}g^{imp}}{(1-f)\kappa^{ice}_{\rm sca} + f\kappa^{imp}_{\rm sca}}, \quad (4)$$

where $\kappa_{\rm ext}$ and $\kappa_{\rm sca}$ are the mass extinction and scattering cross sections, respectively, and the superscripts *ice* and *imp* denote the components for ice and impurity, respectively, f is the mass-fraction of the impurity in unit [ppmw], ρ_s is the snow mass density, and ρ_{imp} is the impurity mass density. For snow impurities, we used a black carbon model [Hess et al., 1998] for the refractive index of the snow impurity (Fig. 13). The snow optical depth for each homogeneous layer within the snowpack is

$$\tau_s^\ell = \tilde{\beta}_{\rm ext}^{ice} h^\ell = \rho_s^\ell \beta_{ext}^{ice,\ell} h^\ell / \rho_{ice} \qquad \text{and} \qquad \beta_{ext}^{ice,\ell} = \frac{3\tilde{Q}_{\rm ext}^\ell (r_{\rm eff}^\ell)}{4 r_{\rm eff}^\ell}, \tag{5}$$

where $r_{\rm eff}^\ell$, ρ_s^ℓ and h^ℓ are the effective snow grain radius, the snow mass density and the thickness of the ℓ^{th} layer. ρ_{ice} is the density of pure ice, and $\tilde{Q}_{\rm e}^\ell(r_{\rm eff}^\ell)$ is the extinction efficiency.

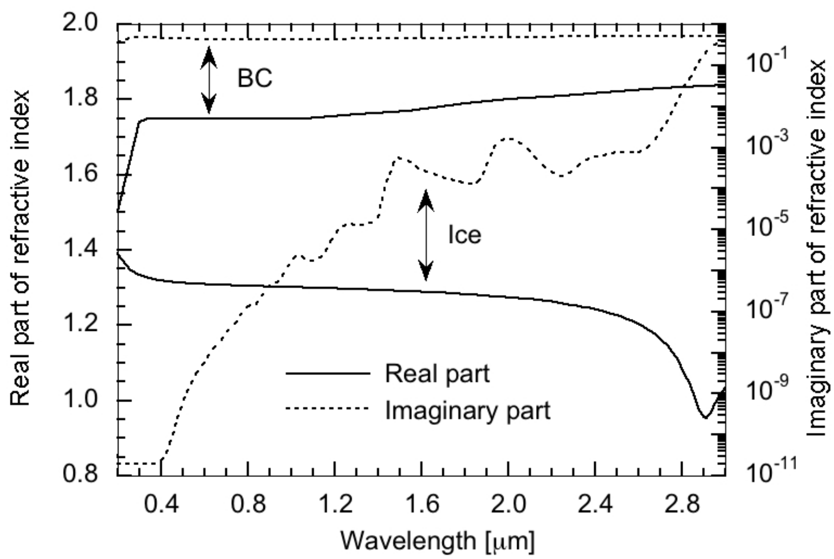

Figure 13: Real and imaginary part of the refractive index of ice [Warren & Brandt, 2008] and black carbon [Hess et al., 1998].

In the previous snow algorithm, we assumed that the snow grains have spherical shapes. A comparison of BRDF measurements obtained by the Cloud Absorption Radiometer (CAR) flown on a NASA aircraft over Elson Lagoon in Barrow, Alaska, see **Fig. 14**, shows that using non-spherical (Voronoi) particle shapes to describe snow grains in our coupled atmosphere-surface radiative transfer model (CRTM) provides a better match with the BRDF measurements than using spherical particles. For the best match, the grain size and impurity are 50 μm and 0.001 PPMW, and the aerosol optical depth is 0.01. These values are consistent with those derived from MODIS data closest in time. This BRDF comparison provides an opportunity to test which scattering phase function yields the best agreement with the measured BRDFs. We found that use of the phase function computed from an assembly of non-spherical Voronoi particles yields a better match with the measured BRDFs than a Henyey-Greenstein phase function with asymmetry factor obtained from Mie computations. We have found that the BRDF produced by an assembly of spherical particles cannot match the measured one, no matter how we adjust the grain size, the impurity concentration or the aerosol properties. This predicament implies that the HG phase function is unsuitable for simulations of the BRDF of snow. Therefore, in year 2015, we updated our snow model to use Voronoi IOPs in order to improve the performance of the snow retrieval algorithms for realistic snow surfaces. The Voronoi particle IOPs has been provided by Dr. Aoki's group using the ellipse ratio M03. Comparisons of retrieved snow grain sizes from MODS data obtained using spherical and Voronoi particle models will be discussed in Section 3.2.2.

Phase function for Voronoi particles In many RTMs an expansion of the phase function in Legendre polynomials is used. This approach requires accurate computation of the expansion coefficients (phase function moments), which is challenging for phase functions with sharp forward peaks occurring for scattering by particles that are large compared to the wavelength. Experimenting with phase functions produced by an assembly of non-spherical Voronoi particles (Ishimoto *et al.*, 2010), we found that special techniques are needed to properly treat such a phase function. Due to the very strong peak in the forward scattering direction, it is very difficult to get the correct phase function moments, needed in the radiative transfer calculations, by numerical integration, and, if handled improperly significant errors will occur. In order to deal with this problem, we experimented with the delta-fit method of Hu *et al.* (2000) and extended it to treat the entire phase matrix. As an example, we show in Fig. 15 all phase matrix elements for a collection of spherical particles computed using a Mie code, and approximated by the delta-fit method. The truncation of the forward peak by the delta-fit method is quite pronounced. Figure 16 shows I, Q, U and V components of the reflected light at the TOA computed by our vector radiative transfer code (VDISORT) using the exact and the delta-fit approximated phase matrices. The good match for all output angles indicates that our delta-fit approximation to the phase matrix elements yields reliable TOA Stokes parameters for reflected light. We then applied the delta-fit method to the phase matrix generated from an assembly of Voronoi particles. As shown in Fig. 17 the phase matrix resulting from application of the delta-fit method closely matches the original phase matrix. Hence, our delta-fit treatment of the Voronoi phase matrix appears to be robust.

Surface elevation correction In cryosphere areas, many places are in high elevation regions, such as Greenland and Antarctica. In these areas, the near surface atmosphere gas distribution will be different from that at sea level. The gas absorption and molecular scattering layer will be thiner, when the elevation is higher. In order to correct the elevation effect, we simulated satellite radiances for different elevations (0–4 km). Then using a neural network technique, we developed a height correction table to convert the satellite measured radiance from any elevation (0–4 km) to the corresponding sea surface radiance. By doing so the snow/ice parameter retrieval algorithm, based on the sea level radiances, could be applied for the retrieval. Figures 18 and 19 show the difference between uncorrected elevation radiance and the sea level radiance. The difference is up to 10-15% at short wavelengths and up to 40% in the NIR, due to the strong Rayleigh scattering at short wavelengths and the strong water vapor absorption in the NIR. The smallest difference is in the 0.865 μm and 1.050 μm channels, since there is weaker absorption and less scattering. So the elevation correction is very important in our snow retrieval algorithm. Figure 20 shows a comparison between corrected sea level radiance and the true sea level radiance. Our correction performance is pretty good. The error in the corrected radiance is within about 0.3%.

Snow layer depth Our algorithm was designed with 2 snow layers to explore the snow vertical structure. Instead of the critical depth used previously, we have fixed the depth of the first snow layer to be 1.5 cm and the second layer to be 98.5 cm. This new snow first layer depth is in the range of 1.64 μm channel penetration depth. Since the 1.64 μm channel has strong snow absorption, and a low S/N ratio, we changed our algorithm to use the 1.05 μm channel instead of the 1.64 μm channel for snow parameter retrieval. An additional benefit is that the 1.05 μm channel is less affected by humidity and surface elevation change than the 1.64 μm channel. In section 3.2, we will apply the new algorithm to MODIS data.

Sea ice model The inherent optical properties (IOPs) of snow can be parametrized in terms of the snow grain size and impurity concentration. Similarly, the IOPs of ice depend on scattering/absorbing inclusions (primarily air bubbles and brine pockets) and impurities embedded in the ice [Jin et al., 1994; Hamre et al., 2004; Jiang et al., 2005; Stamnes et al., 2011]. If we can retrieve information about the size of the snow grains and scattering ice inclusions as well as impurity concentrations, we may use a radiative transfer model for the coupled atmosphere-snow-ice-ocean system (hereafter referred to as CRTM) to compute the snow/ice BRDF and albedo. Assuming that snow grains and ice inclusions can be adequately represented by a collection of spherical particles, we may write the IOPs, *i.e.* the absorption and scattering coefficients and the scattering phase function as

$$\alpha_p(\lambda) = \int_{r_{min}}^{r_{max}} \pi r^2 Q_\alpha(r) n(r) dr \ , \qquad \sigma_p(\lambda) = \int_{r_{min}}^{r_{max}} \pi r^2 Q_\sigma(r) n(r) dr \ , \tag{6}$$

$$p_p(\lambda, \Theta) = \frac{\int_{r_{min}}^{r_{max}} p_p(\lambda, \Theta, r) n(r) dr}{\int_{r_{min}}^{r_{max}} n(r) dr} \ , \tag{7}$$

where the absorption or scattering "efficiency" $Q_\alpha(r)$ or $Q_\sigma(r)$ is defined as the ratio of the absorption or scattering cross section for a spherical particle of radius r to the geometrical cross section πr^2, and $n(r)$ is the particle size distribution. For a specific value of the particle radius r, we can compute $Q_\alpha(r)$, $Q_\sigma(r)$, and $p_p(\lambda, \Theta, r)$ using Lorenz-Mie theory, but the integrations in Eqs. (6)-(7) require knowledge of the particle size distribution $n(r)$ which is usually unknown. Equations (6)-(7) can be considerably simplified by making the following assumptions [Hamre et al., 2004; Stamnes et al., 2011]: (i) The particle distribution is characterized by an effective radius

$$r_{eff} = \frac{\int_{r_{min}}^{r_{max}} n(r) r^3 dr}{\int_{r_{min}}^{r_{max}} n(r) r^2 dr}$$

which obviates the need for an integration over r. (ii) The particles are weakly absorbing, so that

$$Q_\alpha(r) \approx \frac{16\pi \, r_{eff} \, m_{i,p}}{3\lambda} \frac{1}{m_{rel}} [m_{rel}^3 - (m_{rel}^2 - 1)^{3/2}] \tag{8}$$

where $m_{i,p}$ is the imaginary part of the refractive index of the particle, λ is the wavelength in vacuum, and $m_{rel} = m_{r,p}/m_{r,med}$ is the ratio of the real part of the refractive index of the particle ($m_{r,p}$) to that of the surrounding medium ($m_{r,med}$). (iii) The particles are large compared to the wavelength ($2\pi r/\lambda >> 1$) which implies $Q_\sigma(r) = 2$. The scattering phase function may be represented by the one-parameter Henyey-Greenstein (HG) phase function, which depends only on the asymmetry factor

$$g \equiv \langle \cos\Theta \rangle = \frac{1}{2}\int_{-1}^{1} p(\Theta)\cos\Theta \, d(\cos\Theta).$$

With these assumptions, Eqs. (6)-(7) become:

$$\alpha_p(\lambda) = \alpha(\lambda)\frac{1}{m_{rel}}[1-(m_{rel}^2-1)^{3/2}]f_V\ , \qquad \sigma_p(\lambda) = \frac{3}{2}\frac{f_V}{r_{eff}}\ , \tag{9}$$

$$p_p(\lambda,\Theta) = \frac{1-g^2}{(1+g^2-2g\cos\Theta)^{3/2}}. \tag{10}$$

Here $\alpha(\lambda)$ is the absorption coefficient of the material of which the particle is composed, and $f_V \equiv \frac{4\pi}{3}\int n(r)r^3 dr \approx \frac{4}{3}\pi r_{eff}^3 n_e$, where n_e = number of particles per unit volume with radius r_{eff}. As described by Stamnes et al. [2011] this approach can be extended to work very well for wavelengths less than about 2.8 μm.

Aerosol model For aerosol retrieval, we assume a fixed aerosol model in the SGLI snow retrieval algorithm as we did for GLI. But we do consider real humidity information in the aerosol model. Different geographical regions are expected to have different aerosol properties, and all aerosol models will be obtained from the OPAC compilation [Hess et al., 1998]. So only the aerosol optical depth will be retrieved. For the Arctic and Antarctica, we will directly use the OPAC Arctic and Antarctic aerosol models. For mid-latitude regions, there are three types of aerosol models available in OPAC (Continental Average, Continental Clear, Continental Polluted). We are not going to retrieve the relative humidity (RH), instead we will directly use a given (near-real time) RH value (obtained from other satellite data) in our aerosol retrieval. We pre-calculated the IOPs for each aerosol type with RH $= 0\%, 50\%, 70\%, 80\%, 90\%, 95\%, 98\%$, and 99%. Then we linked these 8 humidity values to provide a continuum of aerosol IOPs by using spline interpolation on humidity. The humidity is considered to be a given variable which is used in the forward radiative transfer calculation as well as in our retrieval algorithm. Figure 21 shows the impact of humidity on the TOA radiance. We compare the TOA radiance for RH = 0% humidity with the RH values from 50% to 99%. From Fig. 21, we note that in the visible the RH effect could be 4 - 11%, while in the NIR, this effect is smaller, and about 1 - 4%. These results demonstrate that use of real time RH information will be very important for the snow retrieval because of the large impact on radiances, especially in the visible spectral range.

In our current algorithm, the aerosol model will be selected based on the geographical area [Hess et al., 1998]. The near-real time humidity will be obtained from another sensor, and used in the retrieval code as a given parameter. Thus, the snow and aerosol retrieval will be based on near-real time humidity information. The atmospheric model will be the US standard model.

2.2.2 Neural Network (NN) Training

In order to retrieve the snow and atmospheric parameters simultaneously, we need to use an inversion method. The traditional lookup table (LUT) interpolation method is not suitable for simultaneous and accurate retrieval of multiple parameters. Instead, we use a nonlinear, iterative optimal estimation method [Li et al., 2008]. But this approach is very time consuming because we need to call the forward model repeatedly to compute radiances and Jacobians required in the nonlinear, iterative optimal estimation method described in the next section. In order to solve this problem, we replaced the forward radiative transfer model with a radial basis function neural network (RBF-NN) to establish a relationship between the retrieval parameters (referred to as P) and the spectral radiances (referred to as R). A two-layer RBF-NN was employed here for training of the interpolating radial basis functions.

(a) Spectral radiance to parameters training ($R2P$ training): We start by training a RBF-NN in which the spectral radiances and the solar zenith angles are used as input data, whereas the snow and aerosol parameters are the output data. The benefit of this training is that we can use the results directly to estimate the initial snow and atmospheric parameters for the retrieval. Thus, by using the training coefficients, we can directly calculate the snow and atmospheric parameters given by

$$P_k = \sum_{j=1}^{N} a_{kj} \exp\{-b^2 \sum_{i=1}^{N_r} (R_i - c_{ji})^2\} + d_k, \tag{11}$$

where N is the total number of neurons, and N_r is the sum of the number of input radiances and the number of solar zenith angles. The R_i's are the input parameters, and a_{kj}, b, c_{ji} and d_k are the optimized coefficients.

(b) Parameters to spectral radiance training ($P2R$ training): The purpose of this RBF-NN is to provide a relationship between the retrieval parameters and the radiances and use this analytic relationship to derive an analytic expression for the Jacobians. Both the radiances and the Jacobians are required in the nonlinear optimal estimation described in the next section. The input data are the snow and atmospheric parameters (*i.e.* snow grain size, snow impurity concentration, and aerosol optical depth) and the solar zenith angles. The output data are the radiances in all SGLI channels. The spectral radiance R_i in channel i obtained from the radial basis neural network (RBF-NN) is given as:

$$R_i = \sum_{j=1}^{N} a_{ij} \exp\{-b^2 \sum_{k=1}^{N_p} (P_k - c_{jk})^2\} + d_i, \tag{12}$$

where N and N_p are the total number of neurons and input retrieval parameters, respectively. The P_k's are the input parameters, and a_{ij}, b, c_{jk} and d_i are the optimized coefficients. Note that the radial basis functions functions in Eqs. (11) and (12) are trained on the logarithms of R_i and P_k, and that normalization has been used to adjust the magnitude of the different input parameters, because the magnitudes of grain size and optical depth are quite different.

This difference could decrease the accuracy of the Gaussian radial basis functions [Eq. (12)]. The normalization alleviates this problem.

The Jacobians (partial derivatives) are also required for the retrieval by nonlinear optimal estimation as discussed in the next section. These Jacobians can be calculated by analytical differentiation as follows

$$J_{ik} = -2 \sum_{j=1}^{N} a_{ij} b^2 (P_k - c_{jk}) \exp\{-b^2 \sum_{l=1}^{N_p} (P_l - c_{jl})^2\}. \tag{13}$$

2.2.3 Nonlinear optimal estimation

We use cost function minimization techniques appropriate to nonlinear iterative spectral fitting [Li et al., 2008]. The retrieval parameters are assembled into a state vector $\mathbf{x} = [P_1, P_2, \ldots, P_n]^T$, and the measured radiances into another vector $\mathbf{y}_{meas} = [R_1, R_2, \ldots, R_m]^T$. The update of the state vector $\mathbf{x}_i$ at iteration step i is given by [Rodgers, 2000]:

$$\mathbf{x}_{i+1} = \mathbf{x}_a + \mathbf{G}_i \Big[\mathbf{y}_{meas} - \mathbf{y}_i + \mathbf{K}_i (\mathbf{x}_i - \mathbf{x}_a) \Big] \tag{14}$$

$$\mathbf{G}_i = \mathbf{S}_a \mathbf{K}_i^T (\mathbf{K}_i \mathbf{S}_a \mathbf{K}_i^T + \mathbf{S}_\epsilon)^{-1}. \tag{15}$$

The measurement vector $\mathbf{y}_{meas}$ has covariance matrix $\mathbf{S}_\epsilon$ corresponding to noise ϵ, $\mathbf{y}_i = \mathbf{F}(\mathbf{x}_i, \mathbf{b})$ are simulated radiances generated by the forward model $\mathbf{F}(\mathbf{x}_i, \mathbf{b})$ which is a (non-linear) function of $\mathbf{x}_i$ and $\mathbf{b}$ (vector of model parameters not retrieved but sources of error). $\mathbf{K}_i$ is the Jacobian matrix of simulated radiance partial derivatives with respect to $\mathbf{x}_i$. The *a priori* state vector is $\mathbf{x}_a$, with covariance $\mathbf{S}_a$. $\mathbf{G}_i$ is the gain matrix of contribution functions. The inverse process starts from an initial guess $\mathbf{x}_0$; often set to $\mathbf{x}_a$. A convergence criterion checks progress towards the solution that minimizes the cost function. Besides measurement noise and *a priori* covariance (smoothing error), other sources of error are uncertainties in the elements of $\mathbf{b}$, and forward model uncertainties due to physical and/or mathematical simplifications.

In order to speed up the retrieval, our algorithm used the RBF-NN method instead of the traditional LUT approach. This new algorithm has several benefits:

- We use the information available in all channels to solve the inverse problem by the optimal estimation method to produce simultaneous retrieval of all desired parameters.
- We use the $P2R$ neural network to compute the simulated spectral radiance R^{NN} and Jacobian J^{NN}, which speeds up the retrieval by a factor of 100 or more compared to the LUT appraoch.
- We use the $R2P$ neural network to obtain a good first guess of our retrieval. This approach will effectively decrease the number of iterations required for the optimal estimation algorithm to converge.

2.2.4 Snow and sea ice surface albedo retrieval

In the current algorithm, we provide 2 types of broadband snow albedos and one type of sea-ice broadband albedo in 3 wavelengths ranges (VIS: $0.3 - 0.7$ μm; NIR: $0.7 - 2.8$ μm; SW: $0.3 - 2.8$ μm). For snow covered surfaces, we have 2 ways to compute the broadband albedo: direct albedo and indirect albedo. For sea-ice covered areas, we provide only the direct sea-ice albedo.

Snow indirect albedo From the physical parameters inferred from our snow/ice retrieval algorithms and the corresponding IOPs derived from them, we may use the CRTM to calculate the broadband albedo, the surface BRDF and the spectral albedo of the coupled system. These snow/ice parameters include the snow/ice particle size and the impurity concentration. The broadband snow/ice albedo obtained in this manner is called indirect albedo. It cloud be the black (transparent) sky (if we ignore the atmosphere) or the actual or blue-sky snow/ice albedo (if we include the atmosphere and the retrieved aerosol optical depth), but it is calculated without invoking the Lambertian assumption because the full BRDF of the surface is accounted for in the CRTM. This snow/ice albedo estimate, based on retrieved snow/ice IOPs, provides results that are more accurate than those produced by the standard MODIS broadband albedo algorithm [Li et al., 2007]. In this algorithm, we provide only the broadband albedo for SGLI standard products, but we have the potential to provide the BRDF and spectral albedo too.

Snow direct albedo Although the indirect albedo provide a lot of important information, one key limitation of this indirect albedo estimation is that its accuracy will depend on the accuracy of the retrieved snow parameters. If the retrieved snow grain size and impurity concentrations are inaccurate, the inferred albedo results will be inaccurate too. So how do we validate the retrieved snow grain size and impurity concentration? One option would be to rely on field measurements, but one is limited by the sparsity of field data, which may be available only for a few days of the year at a few locations. Another limitation is that field data do not allow for validation of snow retrievals on a pixel by pixel basis. In view of this space-time sparsity of field measurements and the critical need for validations, we provide another albedo, which called the direct albedo.

The direct albedo approach consists of retrieving the actual snow surface albedo directly from the measured satellite radiances. Using our CRTM for the coupled atmosphere-snow surface system, we can simultaneously simulate the satellite radiances and the snow surface albedo as a function of snow grain size and impurity concentration and aerosol optical depth. These simulations can be used in conjunction with a neural network to estimate directly the surface albedo and the aerosol optical depth from 8 SGLI channels (or 7 MODIS channels). In this manner one obtains the actual snow surface albedo of the coupled atmosphere-snow surface system. Because this actual snow surface albedo is inferred directly from the measured satellite radiances, it is not influenced by inaccuracies in our retrieved snow parameters. This new direct snow albedo algorithm, can be used for fast and accurate broadband snow albedo estimation, and the difference between the old (indirect) and the new (direct) albedo estimations will provide a valuable indicator about the quality of the retrieved snow parameters.

The quality of the retrieved snow parameters depends to a large extent on the performance of the cloud mask and the surface classification algorithm. Inferior quality of the retrieved snow parameters in a given pixel is mainly due to imperfect identification of thin clouds, aerosols, melting snow, ice (instead of snow), or partial vegetation (forest) cover, and lack of removal of these effects in the TOA radiances. For such "fake" snow pixels, which are frequently encountered in satellite images, the TOA radiances do not depend on just pure snow, and the performance of the snow parameter retrieval algorithms is mostly determined by such "fake" snow pixels. To alleviate this problem, we are providing both direct and indirect albedo estimates. By comparing these two albedo estimates we will be able to provide a snow retrieval quality flag for every pixel in an image. Figure 22 is an example of how we can use the difference between the two albedo values to estimate the quality of the retrieved snow parameters. We note that there are many pixels around the edge of Greenland with large relative differences, implying that the retrieved snow parameters are untrustworthy. These areas mostly correspond to the sea-ice or melting snow.

Sea-ice direct albedo In year 2014, we used the CRTM to model the radiative transfer in the coupled atmosphere-sea ice system [Stamnes et al., 2011]. The satellite measured radiance over sea-ice was simulated as a function of the abundance of air bubbles and brine pockets in the sea ice as well as its thickness. The direct albedo was computed in a similar way as described for the snow direct albedo. A neural network technique was used to link the simulated satellite radiance and pre-calculated values of three broadband surface albedos. The simulated radiances were computed for sea ice conditions ranging from new ice, first year ice to multiple year ice. Table 3 lists the sea ice types and ranges used in the simulations. Each of the three sea ice types includes 10,000 simulation cases, which gives total of 30,000 cases for the neural network training. The direct sea ice albedo model (synthetic) data yields a very good retrieval as can be seen in Fig. 23. In next year we will test the sea-ice albedo retrieval algorithm using MODIS data.

Table 3: Sea-ice types and ranges used in the simulations

item	New ice	First-year ice	Multiple-year ice
sea-ice thickness (m)	0.05 - 0.3	0.3 - 1.0	1.0 - 3.0
air bubble volume fraction	0.16 - 0.35	0.11 - 0.24	0.01 - 0.15
brine pocket volume fraction	0.005 - 0.012	0.008 - 0.04	0.012 - 0.07

2.3 C2: Surface temperature retrieval

Based on the GLI snow surface temperature retrieval algorithm, we developed a similar algorithm for the MODIS and the SGLI sensors. A split-window technique was adopted to estimate the surface temperature in the polar regions by using MODIS channels 31 (11 μm) and 32 (12 μm) as well as SGLI channels T1 (10.8 μm) and T2 (12 μm). This algorithm consists of two parts: one is using model emissivities to generate the algorithm, another is based on field-measurements [Hori et al., 2006] to generate the algorithm. Both the sensor's viewing angle and the snow grain size were taken into account in this algorithm. This algorithm could be applied not only to snow-covered sea and land surfaces, but also to a mixture of snow/ice and melt-ponds. It works only under clear-sky conditions. Even though the technique used to create this algorithm is similar to that used in estimating sea and land surface temperatures in general, this algorithm has been developed specifically for the polar regions and for use with SGLI /MODIS measurements.

2.3.1 Background

The Arctic is particularly sensitive to global climate change. Accurate estimate of surface temperature could provide an early signal of climate change. The surface temperature in the polar regions controls sea-ice growth, snow melt, and surface-atmosphere energy exchange. During the past decade, significant progress has been made in estimation of sea surface temperature and snow/ice surface temperature from satellite thermal infrared data. A common approach for estimating surface temperature is to relate satellite data to surface temperature observations with a regression model. A radiative transfer model can be applied to model satellite radiances and brightness temperature. A large set of atmospheric profiles and measured surface temperature will be used to simulate the satellite measurements under a wide range of conditions. The success of the algorithm depends primarily upon the variability of surface and atmospheric characteristics. In order to correct for atmospheric effects, split-window techniques centered around 11 and 12 μm are commonly employed. Such approaches have been used for SST and IST retrieval [Minnett, 1990; Llewellyn-Jones et al., 1984; Barton, 1985; Key & Haefliger, 1992; Key et al., 1997; Wan & Dozier, 1996; Wan, 2008] and they have been applied to AVHRR and ATSR (Along Track Scanning Radiometer) data using two "split-window" infrared channels at approximately 11 and 12 μm. For the SST algorithm an absolute accuracy of 0.5-1 K (root-mean-square error or RMSE) has been obtained [Llewellyn-Jones et al., 1984; McClain et al., 1985]. IST accuracies of 0.3-2.1 K relative to measured or modeled surface temperatures have been reported by Key et al. [1997] using the split-window technique. Land surface temperature (LST) estimation is generally less accurate due to the larger variability of surface conditions [Price, 1983; Wan & Dozier, 1996].

The surface emissivity is defined as the ratio of the actual radiance emitted by a given surface to that emitted by a black body at the same kinetic temperature. It is a key parameter in this split-window technique. The thermal emissivity of snow/ice has an angular and spectral dependency [Dozier & Warren, 1982; Warren, 1982; Hori et al., 2006; Hall et al., 2008]. Also it varies with snow grain size especially at larger grain sizes [Hori et al., 2006; Hall et al., 2008]. The most significant improvement in this version, except for the effect of the sensor angle, is that we made the snow emissivity depend on grain size. The field emissivity data were collected in Japan and Alaska during the year 2002-2004 [Hori et al., 2006]. We keep both the model emissivity version and the field-emissivity version here for research purposes. The model version includes only the sensor angle effect. The coefficients listed in Table 9 are based on the MODIS channels. Since response functions for the SGLI channels are now available, in year 2015, we updated the coefficients based on the response functions for the SGLI channels (see Table 4 - Table 8).

2.3.2 Algorithm description

In this study the MODTRAN radiative transfer model is employed to simulate the radiances measured by the satellite sensor (*e.g.*, SGLI) using the directional snow emissivities that are computed with the DISORT radiative transfer model. Since MODTRAN has a 2 cm^{-1} spectral resolution, it is accurate enough for the purpose of this study. To simulate radiances in SGLI and MODIS thermal channels, daily temperature and humidity profiles are used in the MODTRAN radiative transfer model. Radiosonde ascents over the entire Arctic are taken from the NCEP/NCAR (National Center for Atmospheric Research) Arctic Marine Rawinsonde archive. This data set contains 17,659 reports of ship (marine) rawinsondes (i.e., radiosondes: tracked from the ground by radar to measure variations in wind direction and wind speed with altitude) for the region north of 65°. Its record extends from 1976 to 1996. Sounding data from this NCAR Rawinsonde archive cover different atmospheric conditions (such as those caused by regional and seasonal variations).

The simple approach for atmospheric correction is to measure radiation from a given field of view at two or more window frequencies having different atmospheric absorption. The surface temperature can then be estimated as a linear combination of measured brightness temperatures at these frequencies:

$$T_S = a(\theta) + \sum_{i=1}^{n} b_i(\theta) T_i, \tag{16}$$

where T_S is the measured surface temperature, θ is the satellite scan angle, $a(\theta)$ and $b_i(\theta)$ are scan angle-dependent coefficients, T_i is the measured brightness temperature in each thermal channel i, and n is the total number of channels used. The minimization of errors in the T_S measurements relies on correct choice of the coefficients $a(\theta)$ and $b_i(\theta)$.

There are two ways to determine the coefficients. One approach is to relate satellite observations to surface temperature measurements with a simple regression model. However, for a robust solution a relatively large set of high-quality *in-situ* temperature and satellite data is required. The other approach is the simulation method. A radiative transfer model is used together with a large set of atmospheric profiles to simulate the satellite measurements under a wide range of atmospheric conditions and surface temperatures. The simulated measurements are then used with a set of assigned surface temperature values to derive the coefficients, again by regression analysis.

Instead of computing a different set of coefficients for each scan angle increment, as shown in (16), here we use the equation

$$T_S = a + bT_{11} + c(T_{11} - T_{12}) + d[(T_{11} - T_{12})(\sec\theta - 1)], \tag{17}$$

where T_S is the estimated surface temperature (in K), T_{11} and T_{12} are the brightness temperatures (in K) at 11 μm (SGLI channel T1, MODIS channel 31) and 12 μm (SGLI channel T2, MODIS channel 32), respectively, and θ is the sensor scan angle. The coefficients a, b, c, and

d are derived from multilinear regression. This approach using two "split-window" infrared channels at approximately 11 μm and 12 μm is commonly employed for surface temperature retrieval [Minnett, 1990; Llewellyn-Jones et al., 1984; Barton, 1985; Key & Haefliger, 1992; Key et al., 1997; Wan & Dozier, 1996].

To ensure high accuracy the MODTRAN radiative transfer model is employed for simulating the radiances measured by SGLI/MODIS. In MODTRAN a narrow-band model is used for computing gaseous optical depth from the HITRAN database with wavenumber steps of 1 cm^{-1}, which implies a nominal spectral resolution of 2 cm^{-1} at FWHM (Full Width at Half-Maximum). Multiple scattering is also included in the radiative transfer model by combining MODTRAN and DISORT. For the SGLI and MODIS instruments, since the sensor scan angle lies between 0° and 50° for SGLI and between 0° and 65° for MODIS, our simulations are done for viewing angles in the range of $0° - 65°$. The built-in standard subarctic winter and summer atmospheric profiles including trace gases and the background aerosol model in MODTRAN are used in our simulations. Blanchet & List [1983] showed that the volume extinction coefficient of Arctic haze is generally of the same order of magnitude as for troposphere aerosols. Thus, we use the troposphere background aerosol model instead of Arctic haze. The calculations of the retrieval coefficients in Eq. (17) using both SGLI and MODIS channels are presented in this document for testing and validating the algorithm. The sensor response functions both for SGLI channels T1 and T2 and for MODIS channels 31 and 32 are used to compute radiances at the top of the atmosphere, and the radiances are then converted to brightness temperature by use of the Planck function.

Table 4: The SGLI coefficients in Eq. (17) for model emissivity algorithm.

Temperature range (K)	a	b	c	d	Corr. coef.
$\leq$ 240	-0.9420168	1.003281	2.080047	0.2917113	0.9991578
240 -260	-1.700981	1.006895	1.668042	0.4842514	0.9998550
260-270	-0.5846105	1.003292	1.329147	0.5522773	0.9975470
270 - 275	-3.221689	1.012690	1.455035	0.4839154	0.9915375
$\geq$ 275	2.843076	0.9904238	1.562278	0.4033772	0.9963182

Table 5: The SGLI coefficients in Eq. (17) for fine dendrite snow in field emissivity algorithm.

Temperature range (K)	a	b	c	d	Corr. coef.
$<$ 240	-1.090729	1.004445	2.084182	0.3006721	0.9991575
240 -260	-1.788184	1.007761	1.656945	0.5195864	0.9998645
260-270	-0.5331097	1.003598	1.317247	0.5939672	0.9975812
270 - 275	-3.630045	1.014699	1.441280	0.5123382	0.9904801

Table 6: The SGLI coefficients in Eq. (17) for medium granular snow in field emissivity algorithm.

Temperature range (K)	a	b	c	d	Corr. coef.
< 240	-1.248099	1.005447	2.083595	0.2596135	0.9991561
240 -260	-2.110133	1.009418	1.751293	0.4588805	0.9998040
260-270	-0.7415222	1.004917	1.331195	0.6152086	0.9980019
270 - 275	-4.578181	1.018801	1.415663	0.5270104	0.9942210

Table 7: The SGLI coefficients in Eq. (17) for coarse grain snow in field emissivity algorithm.

Temperature range (K)	a	b	c	d	Corr. coef.
< 240	-1.299243	1.005852	1.927811	0.2369569	0.9991557
240 -260	-2.174245	1.009710	1.758209	0.4572233	0.9998040
260-270	-0.7264020	1.004918	1.348086	0.6092463	0.9980387
270 - 275	-4.302524	1.017884	1.413851	0.5349259	0.9943376

Table 8: The SGLI coefficients in Eq. (17) for sun crust snow in field emissivity algorithm.

Temperature range (K)	a	b	c	d	Corr. coef.
< 240	-0.7152216	1.000973	2.055423	0.1783278	0.9991505
240 -260	-1.733492	1.005832	1.758956	0.3113386	0.9998055
260-270	-1.223238	1.004883	1.373944	0.4460161	0.9981163
270 - 275	-4.154361	1.015466	1.419622	0.4283974	0.9959655

Table 9: The MODIS coefficients in Eq. (17) for model emissivity algorithm.

Temperature range (K)	a	b	c	d	Corr. coef.
≤ 240	-1.624761	1.008296	2.800785	-0.9120480	0.9991578
240 -260	-2.019964	1.009724	2.500067	-1.009879	0.9998550
260-270	-5.224606	1.022082	1.568301	0.1110692	0.9975470
270 - 275	-2.013436	1.009982	1.558308	-1.298285	0.9915375
≥ 275	-0.4194403	1.004087	1.821280	1.644374	0.9963182

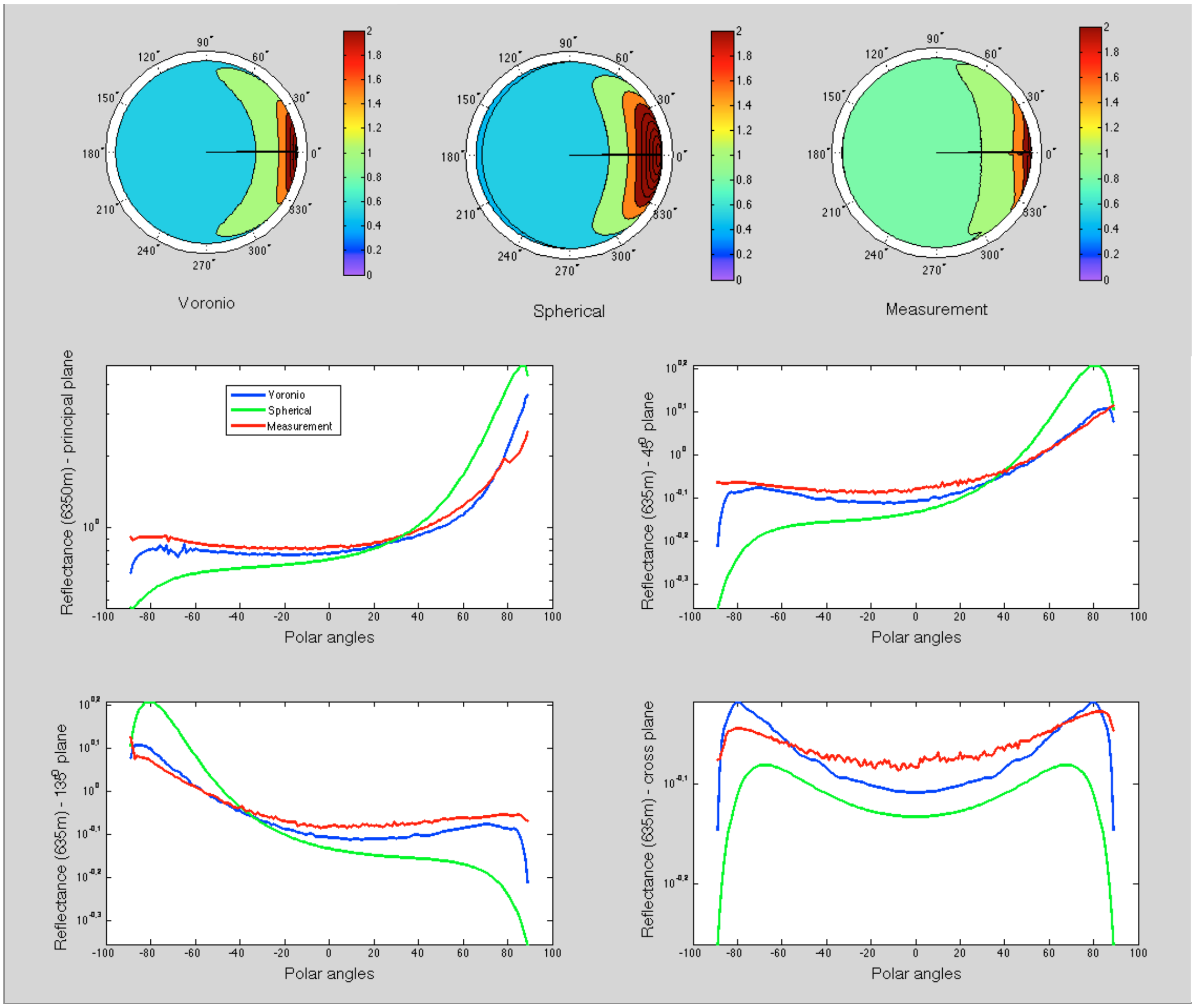

Figure 14: BRDF comparison between snow model simulation (voronio and spherical particle) and CAR measurement over Elson Lagoon, Barrow on April 7, 2008. The modeled BRDF was computed at height 635m, which is the aircraft height. Top 3 panels are the 360^0 BRDF. lower 4 panels are BRDF at principal plane, $45^0, 135^0$ plane and cross plane, separately.

Table 10: The MODIS coefficients in Eq. (17) for fine dendrite snow in field emissivity algorithm.

Temperature range (K)	a	b	c	d	Corr. coef.
< 240	-1.793135	1.009592	2.802395	-0.8154156	0.9991575
240 -260	-2.072019	1.010481	2.503243	-0.9555640	0.9998645
260-270	-4.873211	1.021244	1.713263	-0.3119795	0.9975812
270 - 275	-1.887228	1.010038	1.624779	0.9791106	0.9904801

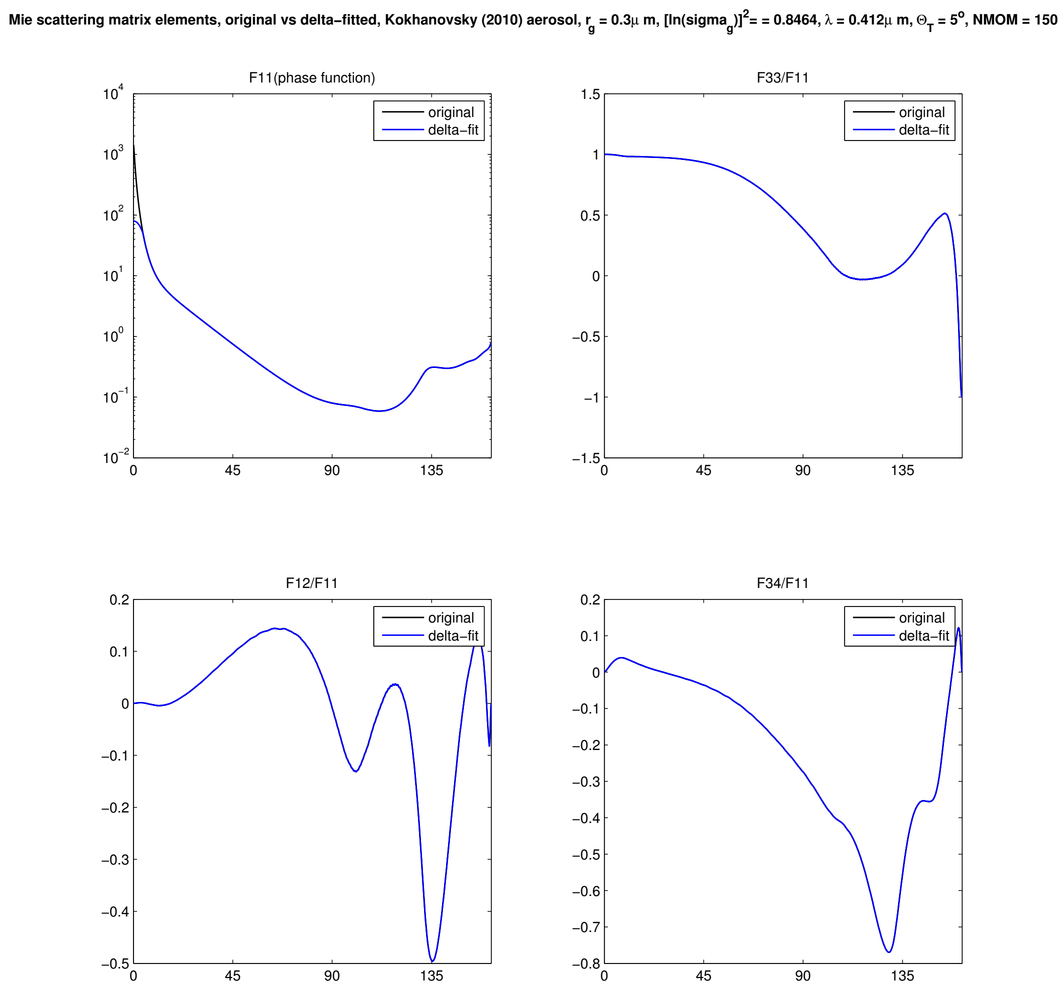

Figure 15: Elements of the Stokes scattering matrix for an ensemble of spherical aerosol particles: Original versus delta-fit approximation.

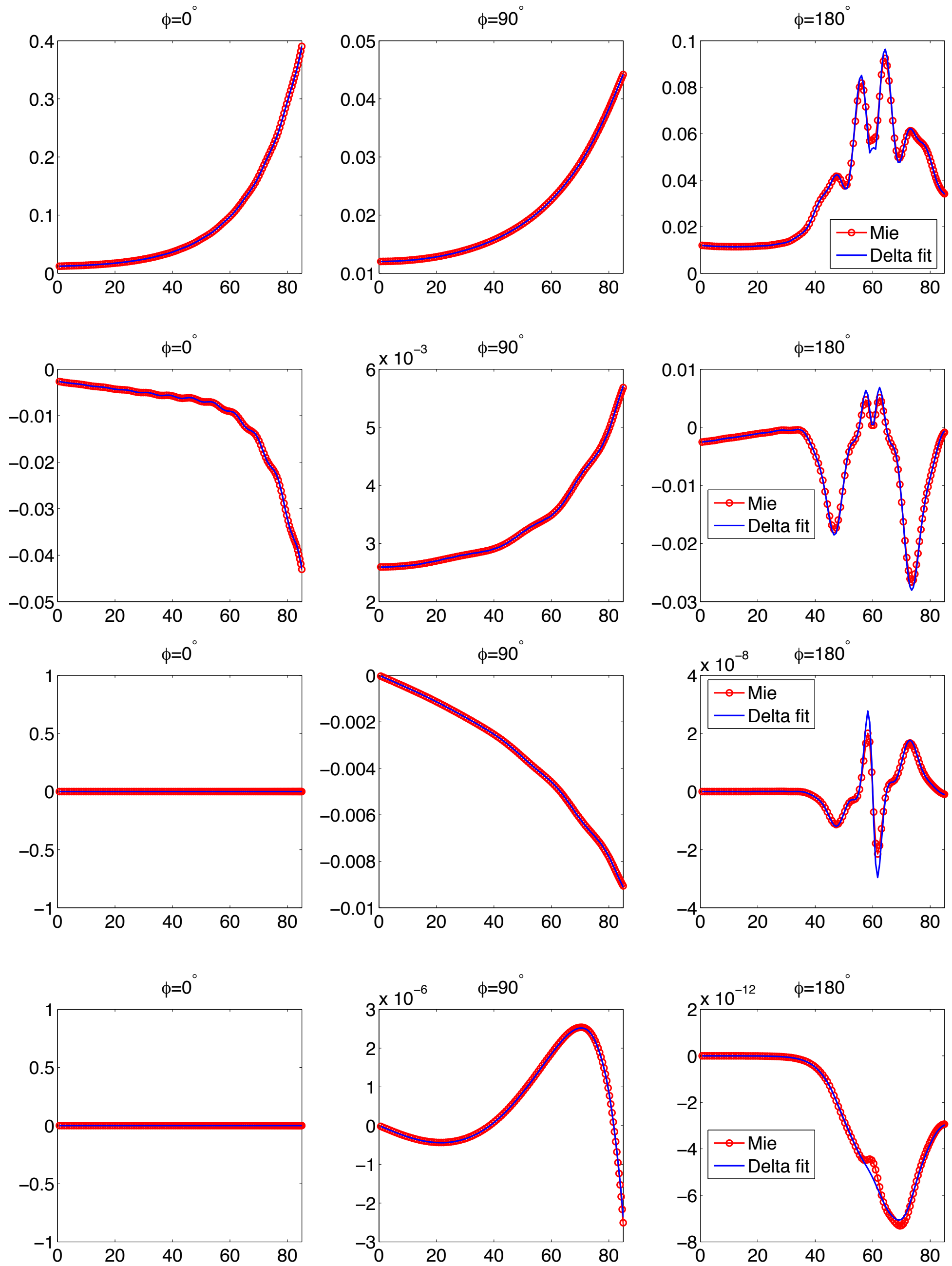

Figure 16: Stokes parameters of reflected light at TOA computed using exact Mie and delta-fit approximated phase matrices. From top to bottom, I, Q, U, and V components. The exact Mie results were obtained using 300 moments whereas 150 moments were used to obtain the delta-fit results.

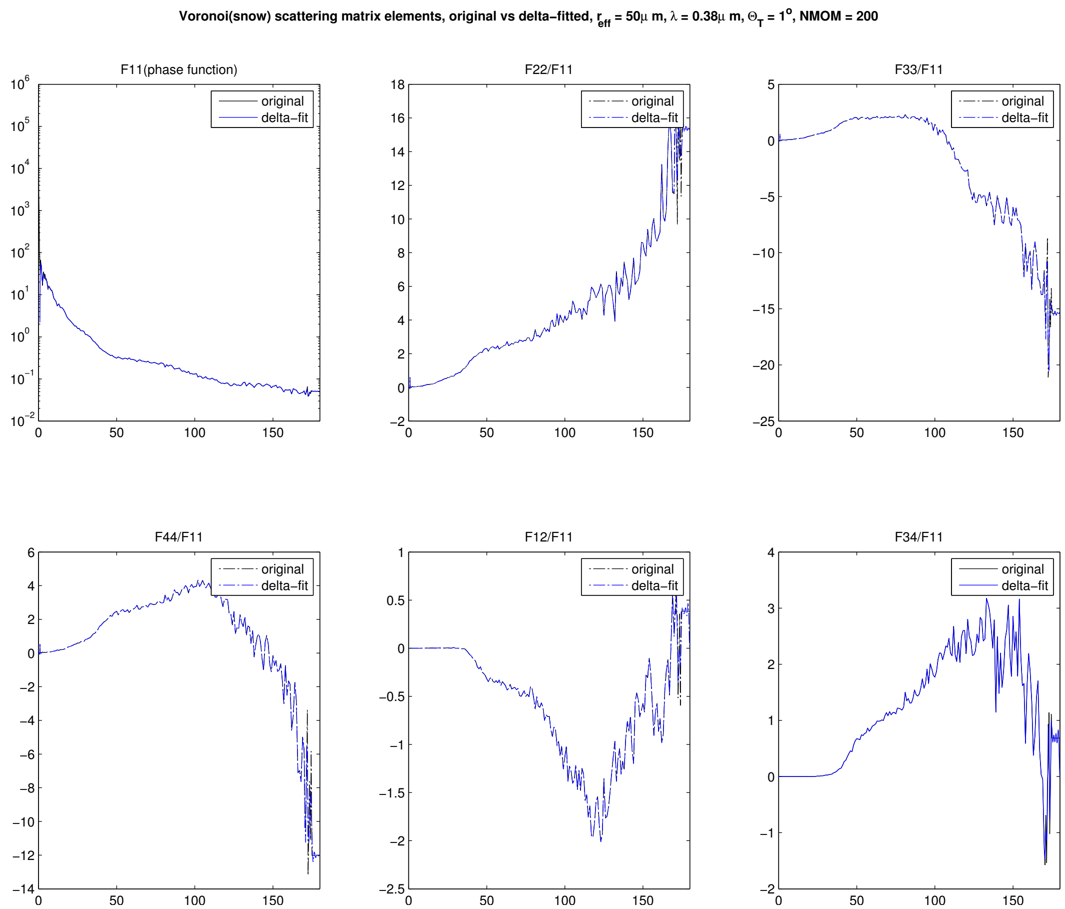

Figure 17: Elements of the Stokes scattering matrix for an ensemble of non-spherical Voronoi particles: Original versus delta-fit approximation.

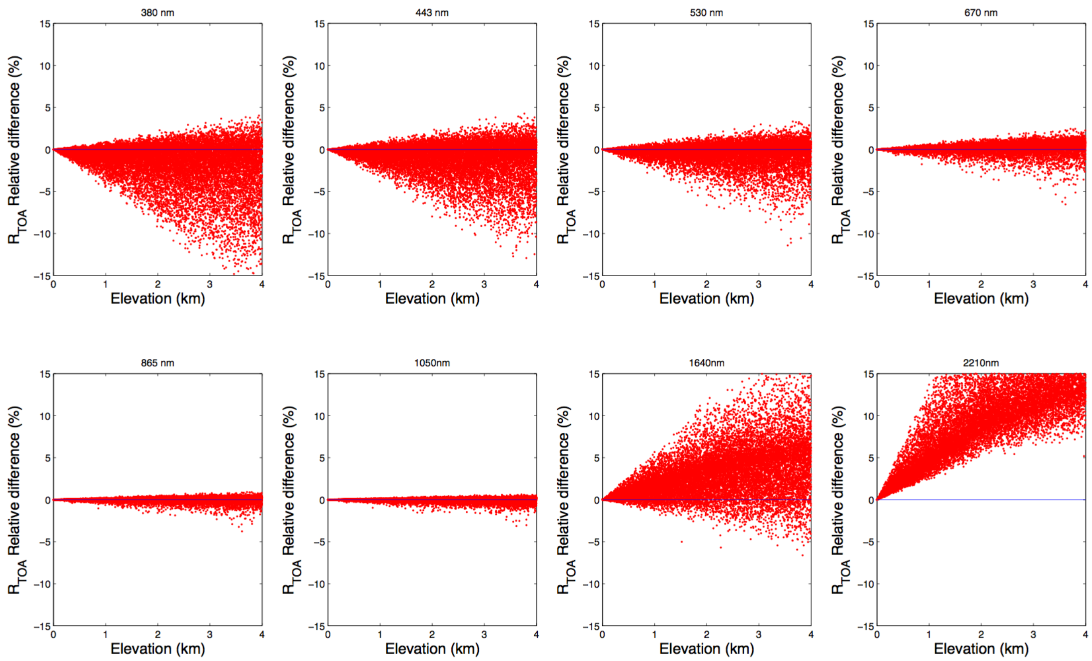

Figure 18: The simulated satellite radiance relative difference (%) between different elevations and sea level.

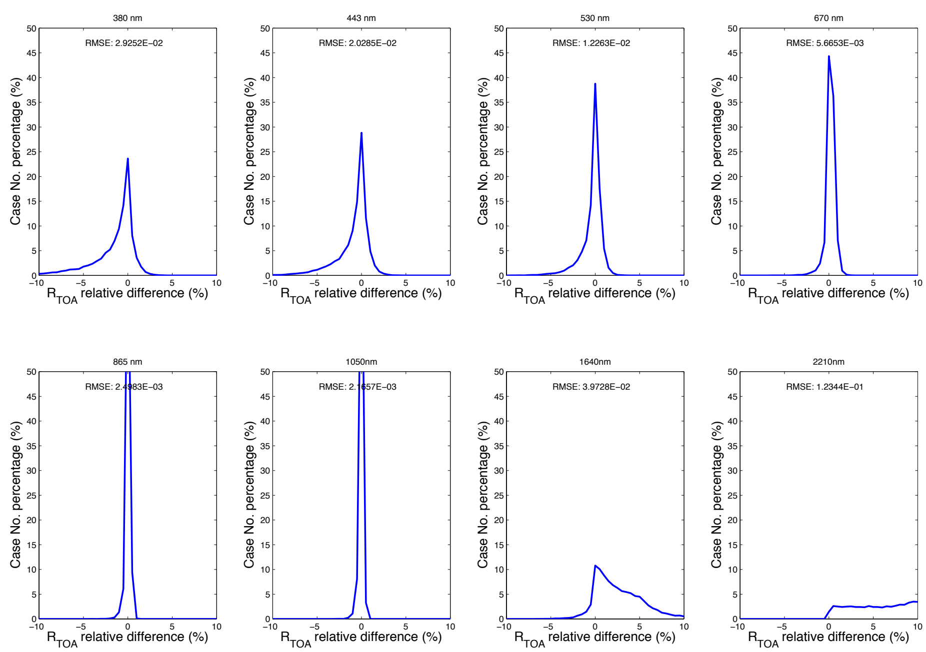

Figure 19: The histogram of simulated satellite radiance difference between uncorrected elevation radiance and sea level radiance.

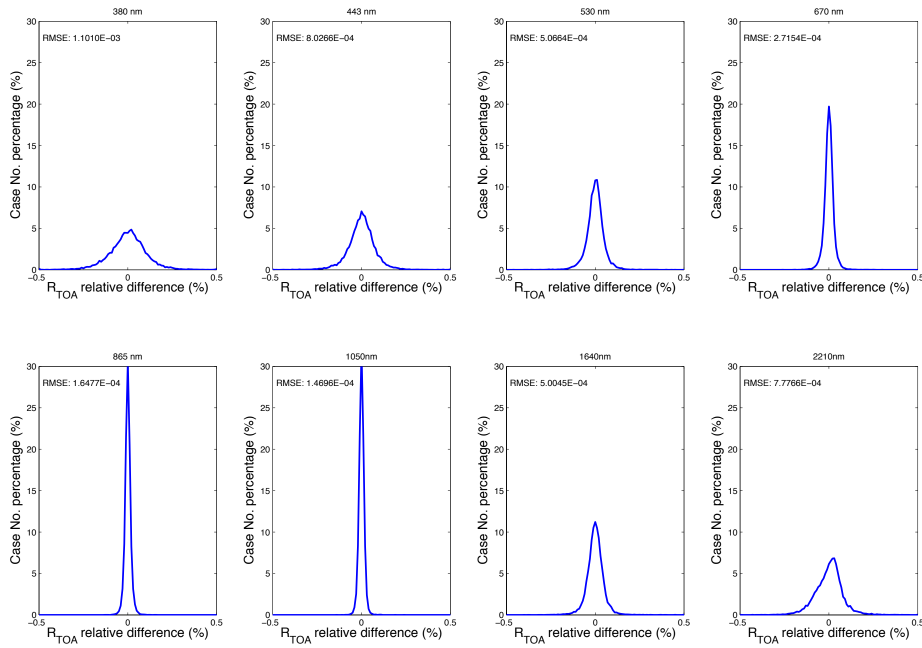

Figure 20: The histogram of simulated satellite radiance difference between corrected sea level radiance vs. the true sea level radiance.

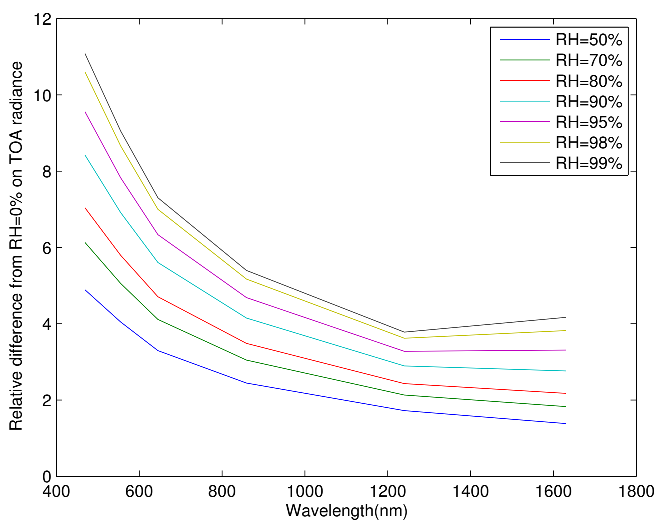

Figure 21: Humidity effect (%) on TOA radiance. Aerosol model: Arctic aerosol from OPAC. Solar zenith angle 50°, sensor zenith angle 65°, relative azimuth 120°, aerosol optical depth 0.08 at 859 nm, first layer grain size 80 μm, second layer grain size 800 μm, impurity 0.01 ppmw.

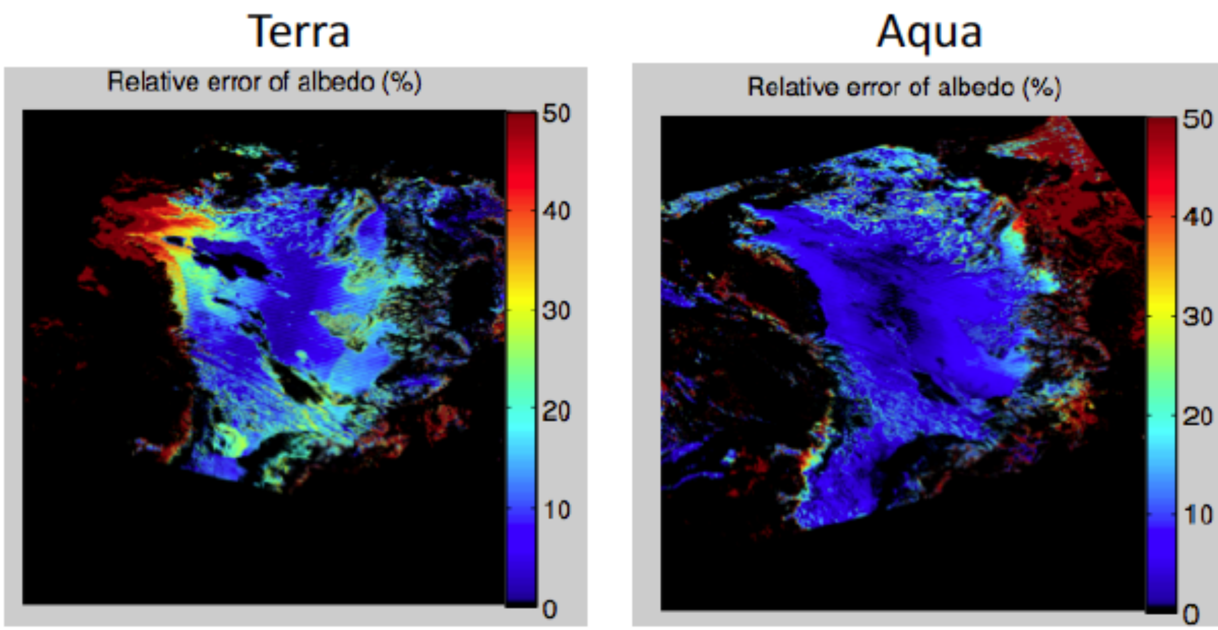

Figure 22: The relative albedo differences between the Terra and Aqua images obtained on June 27, 2012 over Greenland.

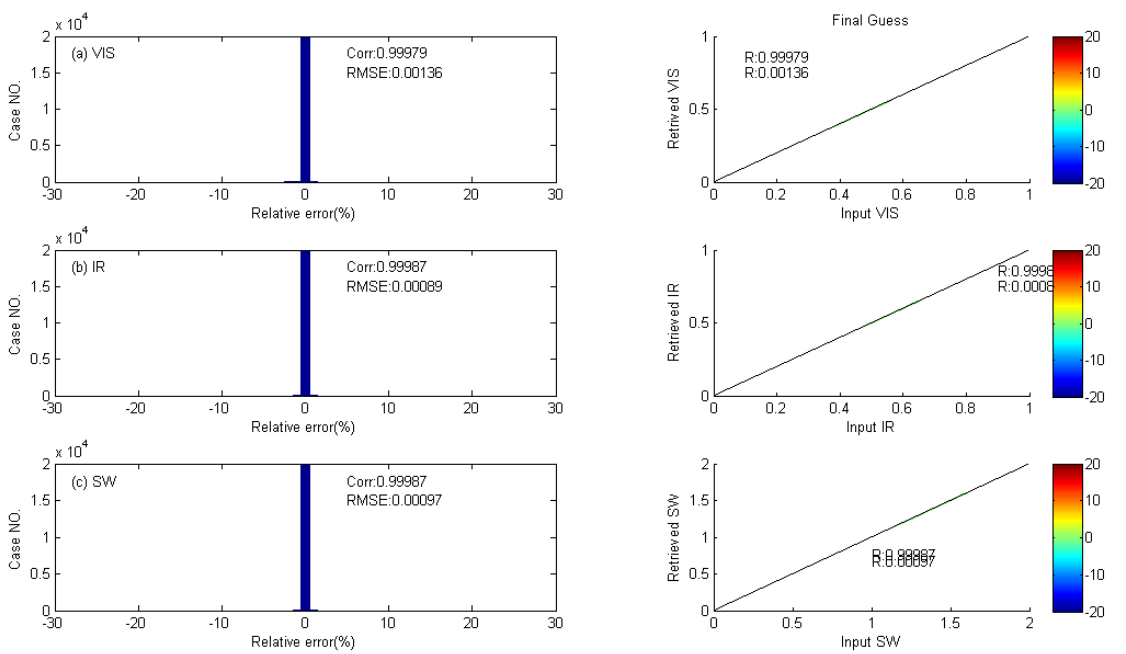

Figure 23: Sea-ice albedo model data retrieval.

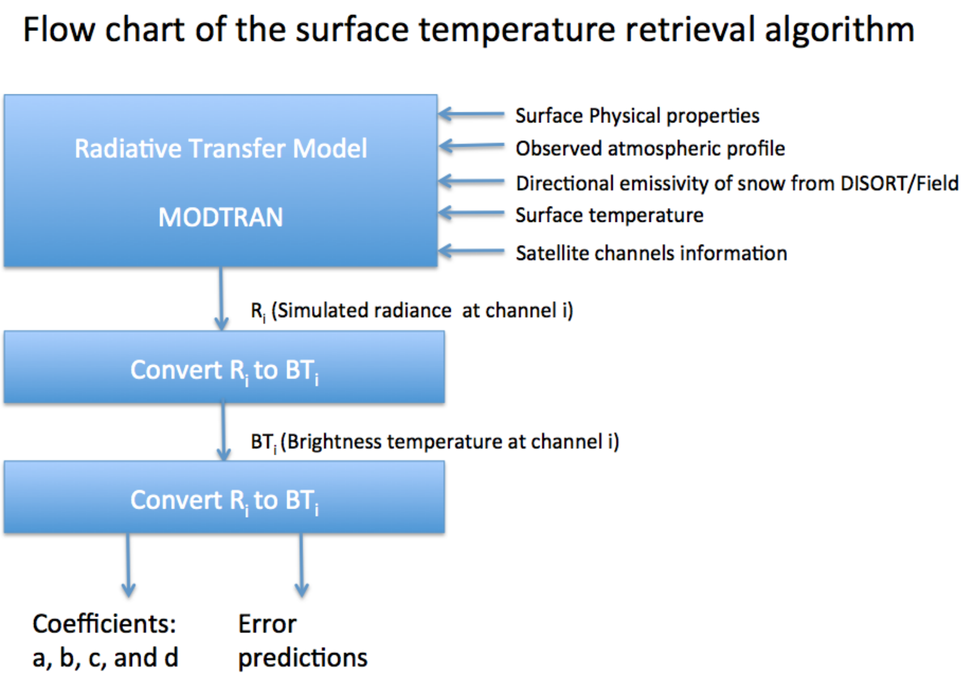

Figure 24: Flow chart of the surface temperature retrieval algorithm.

For the model emissivity version, the directional surface emissivities of snow are calculated based on an extended version of the DISORT radiative transfer model appropriate for the coupled atmosphere-surface system. This algorithm allows us to study the bidirectional reflectance and directional emissivity for a surface covered with different types of snow and sea ice. The coefficients a, b, c, and d in Eq. (17) for SST retrieval are calculated within the following four temperature ranges: (i) $T_{11} \leq 240$ K; (ii) 240 K $\leq T_{11} \leq 260$ K; (iii) 260 K $\leq T_{11} \leq 270$ K; and (iv) 270 K $\leq T_{11} \leq 275$ K.

Table 11: The MODIS coefficients in Eq. (17) for medium granular snow in field emissivity algorithm.

Temperature range (K)	a	b	c	d	Corr. coef.
< 240	-0.9379274	1.004896	2.737998	-1.335196	0.9991561
240 -260	-2.202930	1.010195	2.145490	-0.4138538	0.9998040
260-270	-5.629201	1.023626	1.206063	-1.213855	0.9980019
270 - 275	-2.846899	1.012921	1.494790	1.672925	0.9942210

For the field emissivity version, the field measured emissivity ([Hori et al., 2006]) was used to calculate the coefficients a, b, c, and d. There are 4 different types of snow according to the snow grain size. They are the fine dendrite snow; medium granular snow, coarse grain snow, and sun crust. When the grain size increases, the emissivity decreases. We used the

Table 12: The MODIS coefficients in Eq. (17) for coarse grain snow in field emissivity algorithm.

Temperature range (K)	a	b	c	d	Corr. coef.
< 240	-1.206548	1.006264	2.743953	-1.425086	0.9991557
240 -260	-2.377483	1.011157	2.087973	-0.2680590	0.9998040
260-270	-5.616658	1.023869	1.192855	1.248157	0.9980387
270 - 275	-2.792477	1.013001	1.489832	1.701098	0.9943376

Table 13: The MODIS coefficients in Eq. (17) for sun crust snow in field emissivity algorithm.

Temperature range (K)	a	b	c	d	Corr. coef.
< 240	-1.338066	1.007215	2.738751	-1.453996	0.9991505
240 -260	-2.513868	1.012142	2.012193	-0.1153396	0.9998055
260-270	-5.590907	1.024266	1.125157	1.502457	0.9981163
270 - 275	-3.277824	1.015255	1.484559	1.794687	0.9959655

same four temperature ranges in the model emissivity version for these four snow grain types. So in this version, we first establish to which snow type the retrieved first layer grain size belongs. The second step is to check the brightness temperature at 11 μm, to decide which temperature group to use. The last step is to use Eq. (17) to calculate the temperature.

For temperatures larger than 275 K, we assume that a mixture of snow/ice and melt-ponds occurs. Because we have no field measurement data for this situation, we will use model emissivity. In such cases the surface emissivities are assumed to be an area-weighted sum of snow and water emissivities. The weights are 0.2 for snow and 0.8 for water. Obviously, this approximation could lead to an uncertainty in the estimated surface temperature.

The procedure used to determine the coefficients in Eq. (17) may be summarized as follows (see Fig. 24). The surface physical properties, observed atmospheric profiles, sensor response functions, and snow directional emissivity data, calculated using the DISORT RT model or taken directly from field measurements, are input into MODTRAN to simulate radiances at SGLI/MODIS channels for a wide range of atmospheric conditions. In these simulations, the temperature of the first layer just above the surface is taken to be the surface temperature. The simulated radiances are integrated with the sensor response functions for the SGLI/MODIS channels:

$$R_i = \int_{\lambda_1}^{\lambda_2} R(\lambda)\phi_i(\lambda)d\lambda, \tag{18}$$

where R_i is the simulated radiance, and ϕ_i is the sensor response function for channel i. Then, the integrated, simulated radiances R_i are converted to brightness temperatures T_i. A least-squares multilinear regression is used to determine the coefficients in Eq. (17). The coefficients in Eq. (17) for the MODIS channels are presented in Tables 9-13, respectively. The correlation coefficients between estimated and actual surface temperature are also given in Tables 9-13.

In order to develop an algorithm using the split-window technique specifically for the polar regions, atmospheric profiles from the NCEP/NCAR Arctic Marine Rawinsonde Archive are used for simulating the sensor-measured radiances. More than 7,000 radiosonde profiles are used for the surface temperature algorithm development. The data set from the NCEP/NCAR Arctic Marine Rawinsonde Archive covers a large range of atmospheric conditions including different seasons and different locations across the Arctic.

2.4 Aerosol over snow retrieval by use of polarization channels

Aerosols have a major impact on the radiative energy balance and climate. In view of the scarcity of cryospheric field measurements, satellite remote sensing has a great advantage by providing accurate estimation with good temporal and wide spatial coverage. However, owing to the high brightness of snow surface that dominates the TOA radiance, and the large variation in snow reflectance determined by grain size (snow age and temperature) and embedded impurities, aerosol retrieval over high albedo snow surfaces remains a challenging problem.

In year 2015, we attempted to address this problem by using the information in SGLI non-polarized channels available for snow retrieval to obtain a direct simultaneous fitting of the measured TOA radiances to derive an optimum set of aerosol and snow properties. For this purpose we used a linearized radiative-transfer model for the coupled atmosphere-snow system, in combination with a non-linear, iterative optimal estimation (OE) inverse method for simultaneous retrieval of aerosol and snow properties. In the validation work, we found that the aerosol retrieval result is not as good as desired, because it is difficult to separate the contribution of aerosols to the TOA radiance from that due to snow impurities. Therefore, we tried to add SGLI polarized channels in our simultaneous retrieval to improve the aerosol results, since the polarized signal will be more sensitive to the small aerosol particles than to the large snow particles. We already did some preliminary work using our Vector Radiative Transfer Model (VDISORT: **?**; **?**) to compute the polarized radiance $\mathbf{I} = [I, Q, U, V]^t$ at the TOA. For this purpose we used a standard aerosol model [Hess et al., 1998] and the IOPs of the snow grains were computed either from Mie theory (assuming spherical particles) or by using an assembly of non-spherical Voronoi particles [**?**]. The snow impurities were assumed to consist of soot particles internally mixed with the snow grains.

Figure 25 shows the sensitivity of TOA scalar reflectance

$$R_I = \pi I / \mu_0 F_0$$

and polarized reflectance

$$R_P = \pi \sqrt{Q^2 + U^2} / \mu_0 F_0$$

in the SGLI channel at 0.6735 μm to variations in the soot concentration for a snowpack consisting of Voronoi particles with a fixed grain size of 100 μm. The aerosol model used was OPAC summertime (Hess *et al.*, 1998).

Figure 26 shows a similar sensitivity test for variations in aerosol optical thickness. As expected, the results show that for large snow grains the polarized reflectance is insensitive

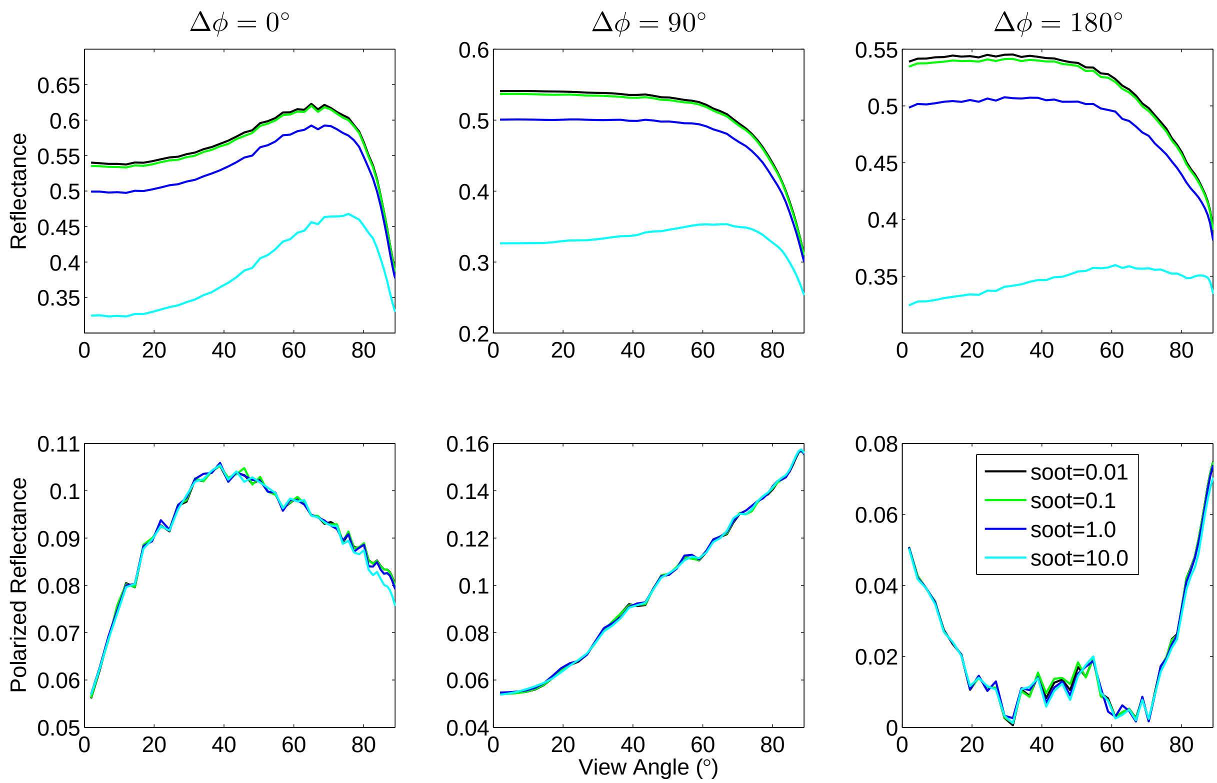

Figure 25: Reflectances for several values of the soot concentration in the snow. Upper panels: scalar reflectance R_I. Lower panels: Polarized reflectance R_P. The aerosol model was from OPAC summertime (Hess *et al.*, 1998) with an optical thickness of 0.05. The solar zenith angle was $\theta_0 = 45°$.

to the soot concentration, whereas the polarized reflectance in the forward direction ($\Delta\phi \in [0°,\ 90°]$) is sensitive to aerosol optical thickness. From this sensitivity study, we can conclude as follows:

- It is not possible to distinguish between AOT (aerosol optical thickness) effects and absorption by snow impurities using radiance-only observations.
- The AOT can be distinguished from snow impurity by using the polarized reflectance.
- The polarized reflectance in the forward direction ($\Delta\phi \in [0°,\ 90°]$) is more sensitive to AOT.

The SGLI polarized sensor is designed to be tilted into the forward scatting direction (”Forward Looking” in the NH and ”Backward Looking” in the SH) (see Fig. 27). Thus, it provides a good opportunity to improve aerosol retrieval over bright snow surfaces by using SGLI's polarization channels. We will continue this work in the next 3 years. We will also explore the advantage of combining the scalar radiance measurements obtained from the other SGLI channels appropriate for retrieval of aerosol/snow properties with the polarized radiances obtained from the two SGLI channels at 0.6735 μm and 0.8685 μm. This approach will also

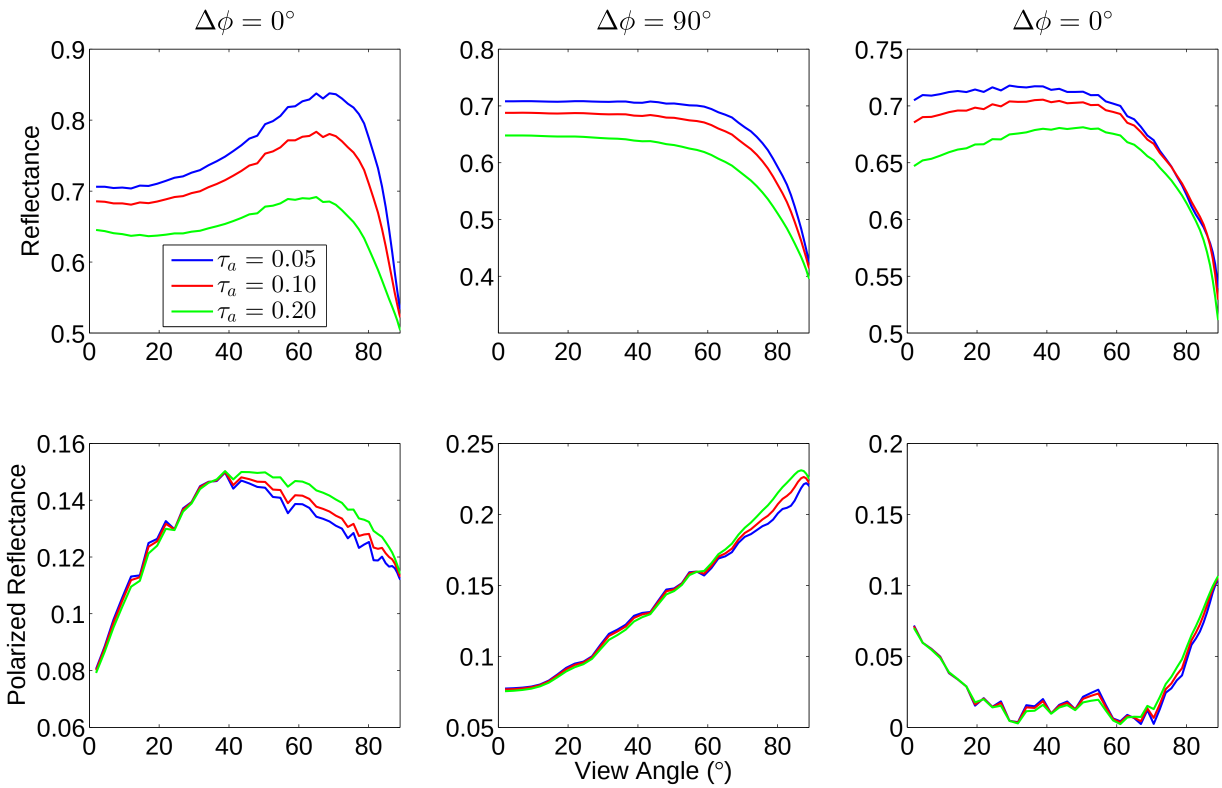

Figure 26: Reflectances for several values of the aerosol optical thickness. Upper panels: scalar reflectance R_I. Lower panels: Polarized reflectance R_P. The aerosol model was from OPAC summertime (Hess *et al.*, 1998 and the snowpack consisted of an ensemble of 100 μm Voronoi particles **externally??** mixed with 1.0 ppm black carbon. The solar zenith angle was $\theta_0 = 45°$.

allow us to use information obtained from multiple angles, which is expected to not only improve the quality of retrieved snow properties, but also help solve the problem associated with the aerosol retrievals over bright surfaces.

3 Algorithm Application and Validation

3.1 Application and validation of the C1 algorithm

We tested our methodology on MODIS data and compared our results with corresponding results produced by the latest version (Collection 6) of the MODIS Cloud Mask (MOD35 and MYD35 for MODIS Terra and Aqua, respectively). In addition to the image-based tests we did a direct comparison of C1 and MYD35 with the CALIOP 1 km cloud layer product for a whole year of data collected over Greenland. This long-term statistical validation using the active cloud detection scheme of CALIOP provides the most reliable assessment currently available of both the C1 and the MODIS cloud masks, and more information can be obtained

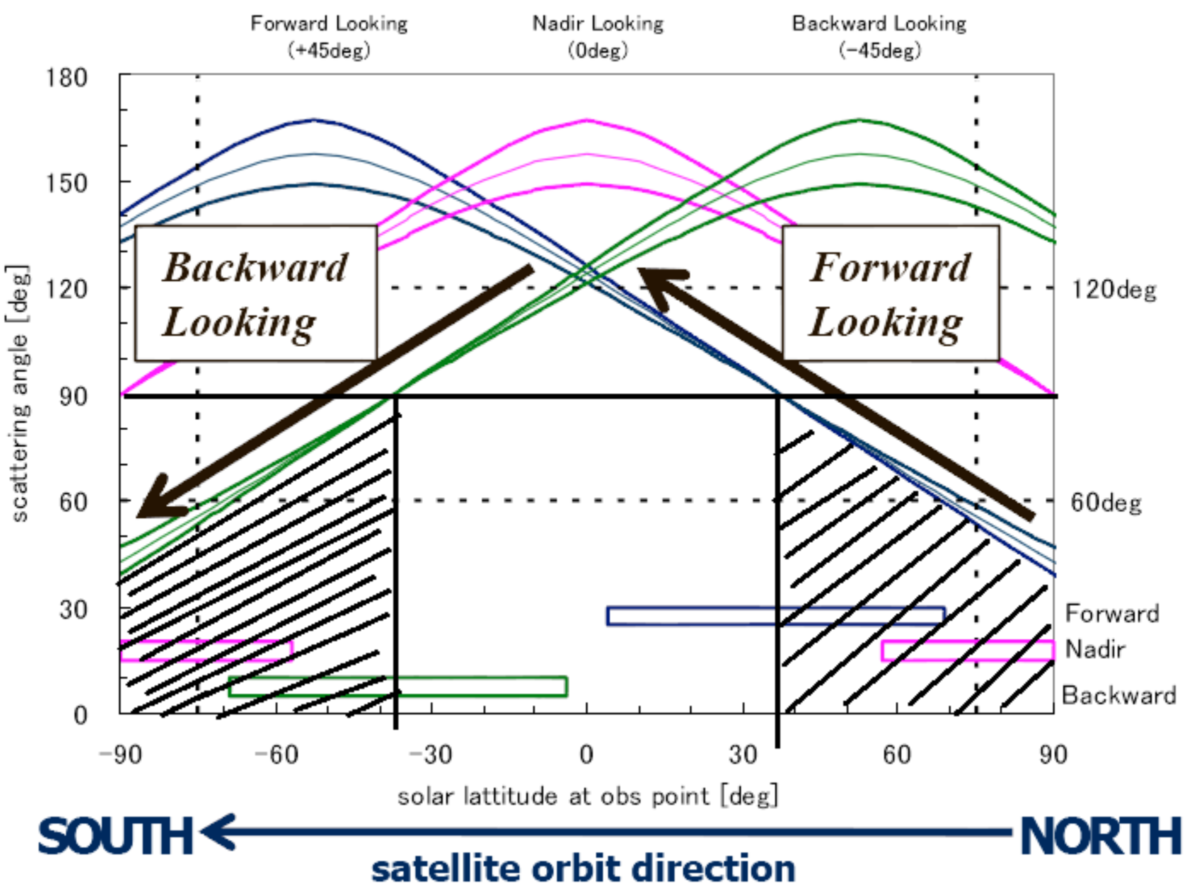

Figure 27: The SGLI polarization sensor orbit direction.

by comparing the results from different seasons. Data from year 2007 were chosen since this year is the first year for which CALIOP has a whole year of observations over Greenland, since CALIOP onboard the CALIPSO satellite was launched April 28, 2006. Only land pixels were included in the statistics since we want to focus on the Greenland land area. The blue bands of MODIS Terra are continually degrading at a faster rate than those of MODIS Aqua. We therefore want to use old data not influenced by this degradation to avoid its impact on C1's NDSI snow identifier. From June 1 to August 10 we used the Sub-Arctic Summer atmospheric constituent profiles [Anderson et al., 1986] in the dynamic threshold calculation whereas the Sub-Arctic Winter profiles were chosen for the rest of the year. In the tests we configured C1 to use different SWIR channels for the MODIS sensors on Terra and Aqua:

1. MODIS channel 6 (1.64 μm) and channel 7 (2.13 μm) were used in the test with MODIS Terra data. Since these two channels are close to SGLI channels SW3 (1.63 μm) and SW4 (2.20 μm) we consider tests with MODIS Terra data to be a simulation of C1's performance on the future SGLI sensor.

2. MODIS channel 5 (1.24 μm) and channel 7 (2.13 μm) were used with MODIS Aqua data due to the detector problem of MODIS Aqua channel 6. MODIS Aqua data can be collocated with CALIOP measurements. Hence, we can use CALIOP as a benchmark to evaluate the performance of our algorithm. Also it would be interesting to see how it performs using different SWIR channels and we consider it a good way to test our methodology.

3.1.1 Image-based tests over Greenland

As a cloud mask designed to work in the polar regions, one of the main targets of the C1 algorithm is that it should deliver reliable cloud mask results over Greenland, which is one of the most difficult places for a cloud mask algorithm because of the high altitude of the Greenland ice sheet and the extremely low surface temperature. Figure 28 shows a comparison between C1 and MOD35 over Greenland with the northwest coast of Greenland (Qaanaaq and Peary land) located at the upper left corner of each panel. In the color composite, the 0.65 μm band is assigned to the red, the 1.6 μm band to the green and the 12.0 μm band to the blue. The clouds are usually in yellow (low-level water clouds), white (mid-level water clouds), orange or red (thick ice clouds with low cloud top temperature) and sometimes blue (thin ice clouds). Snow areas are usually shown in magenta. In the cloud mask results (bottom panels) clouds with cloudy confidence levels from low (dark gray, 66% $<$ clear confidence level $\leq$ 99%), medium (gray, 33% $<$ clear confidence level $\leq$ 66%) to high (white, clear confidence level $<$ 33%, mostly cloudy) are plotted together with snow (red), sea ice (purple), open land (green) and open ocean (blue). For MODIS Cloud Mask results the "confidently cloudy" and "probably cloudy" categories are treated as cloudy scenes and "confidently clear" and "probably clear" are treated as clear scenes. In the circled part of the image areas with thick ice clouds are apparent from either the RGB or the 11 μm BT plots (very low temperatures). MOD35 (lower left) mis-classified this area as snow, while C1 (lower right) correctly masked out this cloudy area. Our tests indicate that in the polar regions the MODIS cloud mask will sometimes miss some of the cirrus clouds or multi-layer clouds with very low temperature. The drastic temperature change during daytime and temperature inversions may create problems for the BT and BTD tests, whereas the reflectance-based scheme of our algorithm is largely unaffected by temperature effects.

3.1.2 Direct comparison with CALIOP using MODIS Aqua data

The launch of NASA's Cloud Aerosol Lidar and Infrared Pathfinder Satellite Observation (CALIPSO) satellite with its onboard CALIOP instrument provides vertically resolved cloud and aerosol information. When accurately collocated with MODIS Aqua measurements CALIOP can provide valuable evaluation of the cloud mask performance of C1 and MYD35 from an active cloud detection perspective. Liu et al. [2010] used CALIOP data to evaluate the accuracy of MODIS Cloud Mask products over Arctic sea ice and found that the MODIS Cloud Mask generally performs better over open ocean than over Arctic sea ice surfaces. In our study we are focusing on the Arctic region and on the Greenland plateau, in particular. The collocated data from CALIOP and MODIS Aqua was taken from March to October of 2007 and the collocation method presented by Holz et al. [2008] was used. We chose to start our comparison from March and end by October because C1 is a daytime algorithm and there is very little data in the Winter season. We are taking the results from CALIOP as the 'truth' to assess the performance of C1 and MYD35. Some detailed statistics of the hit rate and the Hanssen-Kuipers Skill Score or True Skill Score (TSS) [Hanssen & Kuipers, 1965] from three time periods in 2007 are shown in Table 14. The hit rate is defined as:

$$\text{Hit rate} = \frac{N_{cld,hit} + N_{clr,hit}}{N_{total}} \tag{19}$$

where $N_{cld,hit}$ is the number of pixels for which C1 or MYD35 agreed with CALIOP that a cloud was detected, and $N_{clr,hit}$ is the number of pixels for which they agreed that clear-sky was detected and $N_{total} = N_{cld,hit} + N_{cld,miss} + N_{clr,hit} + N_{clr,miss}$ is the total number of MODIS Aqua pixels collocated with CALIOP measurements, including pixels for which the two algorithms disagreed. The TSS defined as:

$$\text{TSS} = \frac{(N_{cld,hit} \cdot N_{clr,hit} - N_{cld,miss} \cdot N_{clr,miss})}{(N_{cld,hit} + N_{cld,miss}) \cdot (N_{clr,hit} + N_{clr,miss})} \tag{20}$$

is widely used to evaluate the effectiveness of a prediction. It provides useful information of the hit rate with respect to the false alarm rate (miss rate), and will remain positive as long as the hit rate is higher than the false alarm rate. A higher TSS means a more reliable prediction and identification from the algorithm. Figure 29 shows a comparison of hit rates and TSS obtained for C1 and MYD35 using CALIOP 1 km cloud layer results as a benchmark. From the statistics we see that C1's performance is generally better than that of MYD35 especially from late-Spring to mid-Autumn with higher hit rate and TSS score. In early Spring (March, April)/late Autumn (October) C1 and MYD35 perform very similarly, but C1 generally has a higher hit rate but slightly lower TSS, indicating a higher false alarm rate. We checked images from the above seasons and found that our algorithm would produce

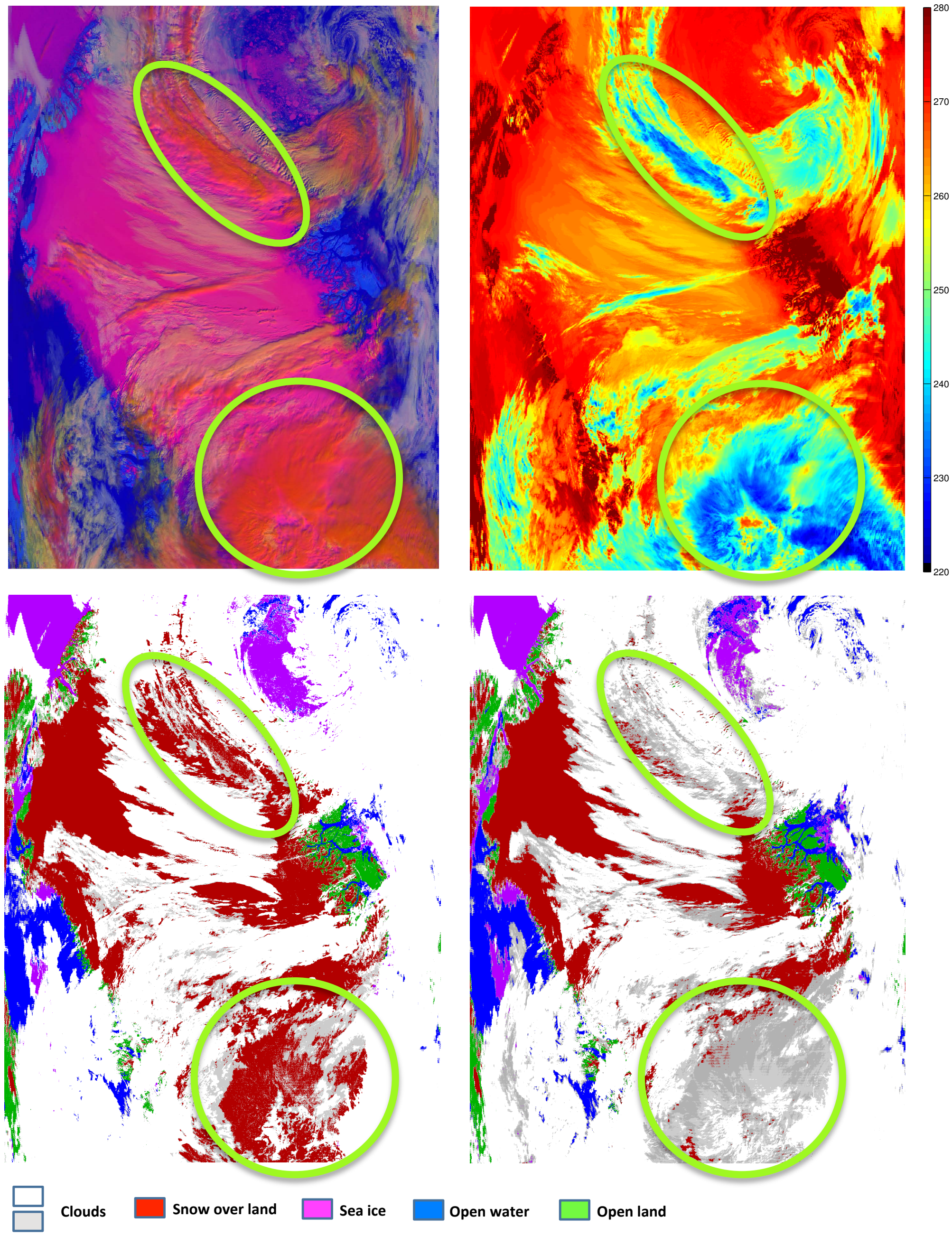

Figure 28: C1 vs. MOD35 Collection 6 (MOD35 C6) for a Terra MODIS image, obtained on July 29, 2005 over Greenland. Upper left: False color RGB composite using MODIS band 1 (0.65 μm) for red, band 6 (1.6 μm) for green, and band 32 (12 μm) for blue. Upper right: 11 μm brightness temperature, note the thick ice clouds with very low temperature ($\approx$ 220-240 K) in circled areas. Lower left: The MOD35 C6 cloud mask. Lower right: The C1 cloud mask.

more false clouds compared to the middle part of the year. Since the atmosphere over the Greenland plateau can become very dry with large variations in specific humidity during Spring and late Autumn [Ettema et al., 2010], use of a fixed atmospheric profile (Sub-Arctic Winter) may account for the higher false cloudy rate in these seasons. However, a small grain size due to surface frost or diamond dust near the snow surface [Grenfell & Warren, 1999b], and the effect of surface roughness (sastrugi) under large solar zenith angles [Warren et al., 1998; Kuchiki et al., 2011], may also contribute to the high false cloudy rate.

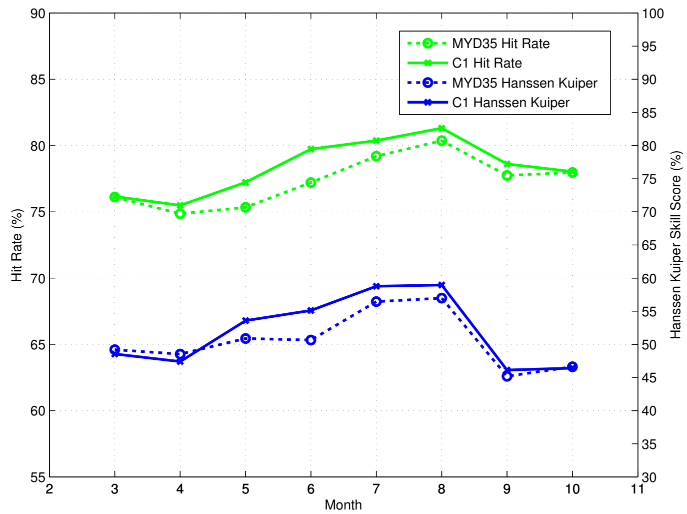

Figure 29: C1 and MYD35 Collection 6 (MYD35 C6) vs. CALIOP over Greenland, 2007.

Table 14: C1 and MYD35 vs CALIOP in Greenland, 2007

Time period	Total matchups	MYD35 HR[a] (%)	C1 HR (%)	MYD35 TSS[b] (%)	C1 TSS (%)
Mar. 01 to May 15	535283	69.34	70.64	40.71	42.03
May 15 to Aug. 23	1291045	74.66	76.90	49.97	53.78
Aug. 23 to Oct. 31	289405	73.69	74.34	42.21	42.44
Overall	2115733	73.18	74.96	47.08	49.76

3.1.3 Cross comparison of C1 using MODIS Terra and Aqua data

As mentioned above, the C1 algorithm is designed for SGLI implying that tests using MODIS Terra data would be the best way to assess its performance on data to be collected with the SGLI sensor since both sensors have the 1.64 μm band available. However MODIS Terra cannot be collocated with CALIOP so there is no direct way to evaluate the performance of C1 using the 1.64 μm channel. As a substitute we compared the cloud fraction over Greenland derived from C1 using both MODIS Aqua and Terra data. If the cloud fractions derived by C1 from the two sensors are close at the same time period of the year, then we may consider it to be an indirect validation of the performance of C1 on MODIS Terra data. Figure 30 shows the 4-day averaged (using data from day 1-4, 5-8, 9-12, etc.) cloud fraction over Greenland in 2007. The cloud fraction is calculated as: $f_{cld} = N_{cld}/(N_{cld} + N_{clr})$ where N_{cld} is the total number of pixels classified as cloudy and N_{clr} is the number of pixels classified as clear by the algorithm during that period. It can be seen that the cloud fractions derived by C1 from the two sensors are generally very close throughout the entire year, indicating that the performances of C1 using the 1.64 μm channel on MODIS Terra and the 1.24 μm on MODIS Aqua are comparable. Larger difference is observed in the Spring season as Terra's cloud fraction is lower than that of Aqua by about 5%, which may be related to the high false cloudy rate obtained when using MODIS Aqua data as discussed in Section 3.1.2. Since the higher degree polynomials needed for interpolation of the 1.24 μm channel on Aqua may introduce larger error in our algorithm, we consider the results obtained from Terra data to be closer to the actual cloud fraction in the Spring season.

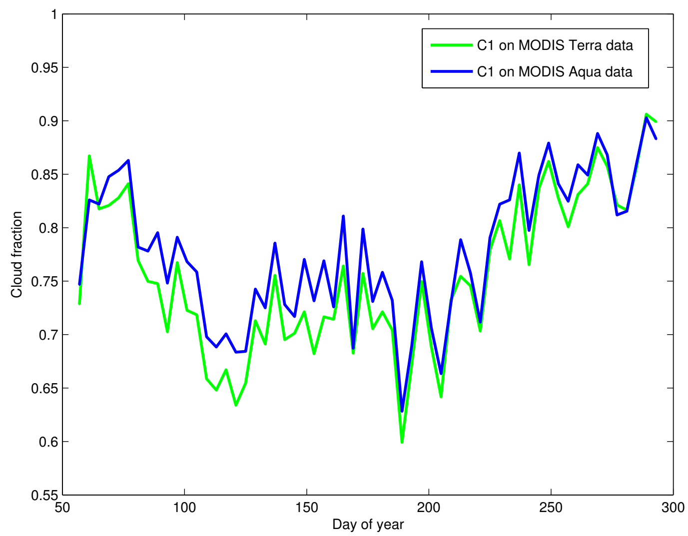

Figure 30: C1 derived 4-day averaged cloud fraction over Greenland, 2007.

3.1.4 Summary

Multi-spectral satellite instruments like AVHRR, MODIS and VIIRS provide high spatial resolution observations over the entire Arctic region. Their data products can be used to derive useful information such as cloud fraction and distribution, snow/ice coverage, surface temperature etc. which will help us better understand Arctic climate and its variability. An accurate cloud mask over the Arctic region is critical in order to obtain reliable products from satellite data. The traditional methods include thermal IR based cloud tests ($BT_{6.7}$, $BTD_{3.7-11}$ etc.) and reflectance-based cloud tests (employing combinations of VIS/SWIR tests with simple solar/viewing geometry correction). Water vapor bands like the 7.2 μm band and the carbon dioxide band at 14.2 μm are also applied to provide additional information. In some of these studies radiative transfer calculations were performed to determine the cloud screening thresholds by simulating different kinds of clouds for a variety of different atmospheric and surface conditions in the Arctic.

The C1 algorithm is developed specifically for the SGLI sensor, which has very few thermal IR channels available. A cloud screening scheme that mainly uses the reflectance of two SWIR channels is established. Compared to other reflectance-based cloud screening methods the thresholds of our method are dynamically determined by the solar/viewing geometry for each satellite pixel based on comprehensive radiative transfer calculations that take into account (snow) surface BRDF, surface elevation and the atmospheric profiles of scattering/absorbing molecules. Compared to the traditional thermal IR based methods our scheme has the following advantages:

1. The thresholds are less sensitive to the drastic temperature changes and frequent temperature inversions occurring in the Arctic.

2. The reflectance thresholds are based on computed snow surface reflectance rather than cloud properties since it is difficult to simulate every possible cloud configuration that may occur under complex atmospheric and surface conditions in the Arctic.

3. A smaller number of satellite channels is required for desirable performance. Sensors with no water vapor and carbon dioxide channels should be able to benefit from a cloud mask similar to C1.

The validation of our cloud masking scheme was performed using data from MODIS Terra, Aqua and CALIOP over Greenland in 2007. The image-based tests show that our algorithm improves the detection of cold ice clouds and cloud edges compared to the thermal IR based MODIS Cloud Mask algorithm. Statistical validation with CALIOP on MODIS Aqua data shows that our C1 cloud mask generally has a higher hit rate and a higher TSS score than the MODIS cloud mask. The cloud fraction derived using MODIS Terra and Aqua data shows that the two configurations of our algorithm using different SWIR channels (1.64 μm and 2.13 μm for MODIS Terra data, 1.24 μm and 2.13 μm for MODIS Aqua data) lead to consistent performance. More work is needed for the early Spring and late Autumn over Greenland since a higher false cloudy rate is observed. Appropriate profile information of the atmospheric absorption for each SWIR channel may be required because a fixed model atmosphere is expected to provide an inadequate representation of the atmospheric conditions over Greenland in all seasons. This problem may be addressed by using surface specific humidity data from the AWS sites on Greenland to correct the standard model atmosphere. Results from the water vapor channels of MODIS would also be helpful. Another possible source of error might be the presence of optically thin ice clouds (τ = 0.1 - 0.5) over Greenland in these seasons which presents a challenge to C1 and other reflectance-based cloud mask algorithms. As indicated by our model calculations the reflectances of these clouds depend strongly on the 'background' surface reflectances and detailed simulations using well-defined surface properties (like snow with different grain sizes) might be a good way to proceed. Other possible sources of mis-classification include surface frost, diamond dust, sastrugi and surface slope. Data from the VIIRS instrument, which has SWIR channels very similar to those of SGLI, and which can be collocated with CALIOP observations, would be very useful for further assessment of the performance of our C1 algorithm. Our existing test and validation framework can easily be adjusted for application to VIIRS data.

3.2 Application and validation of the C2 algorithm

3.2.1 Comparison with GLI algorithms and field measurements

We compared the SGLI algorithm results with the GLI algorithm for the same MODIS images. All these MODIS images corresponded to field measurement data. Aoki et al. [2007a] describe in some the detail the snow pit work for all the field data. For each snow pit work site, we calculated all the satellite pixels within 1 km circle, and then we used the averaged retrieval data of these pixels to compare with the field measurements. The purposes of our work here are (1) to validate our new SGLI algorithm including retrieval feasibility and accuracy, (2) to compare with GLI results to highlight improvements, and (3) to discuss how to improve the next version of this algorithm. Figure 31 shows the snow grain size comparison. The SGLI algorithm retrieval results are shown in the top panels and GLI results in the bottom panels. Both first layer (left panels) and second layer (right panels) snow grain sizes were compared with the field measured data. The field measurements have the measured grain size range, so we plotted the measurement range here for comparison. From Fig. 31 we see that SGLI has more data, which means that the SGLI algorithm retrieved all available MODIS pixels around the field measurement site. But for the GLI algorithm the retrieval failed for some of these pixels. Thus, the SGLI algorithm has a much better retrieval capability than the GLI algorithm. This superior performance could be due to the fact that the SGLI algorithm is based on a nonlinear inverse method which uses the radiance in all channels simultaneously. We used different colors to indicate the data for different snow pit sites, as well as wet snow and dry snow marked by "*" and "o". Most retrieved snow grain sizes lie in the measurement range, but the performance is better for dry snow than for wet snow. For wet snow, actually that is the case in Nakashibetsu. As we discussed in Section 4.2, due to high reflectance from a "sun crust" surface, we got underestimated grain size for the top layer and overestimated grain size for the bottom layer.

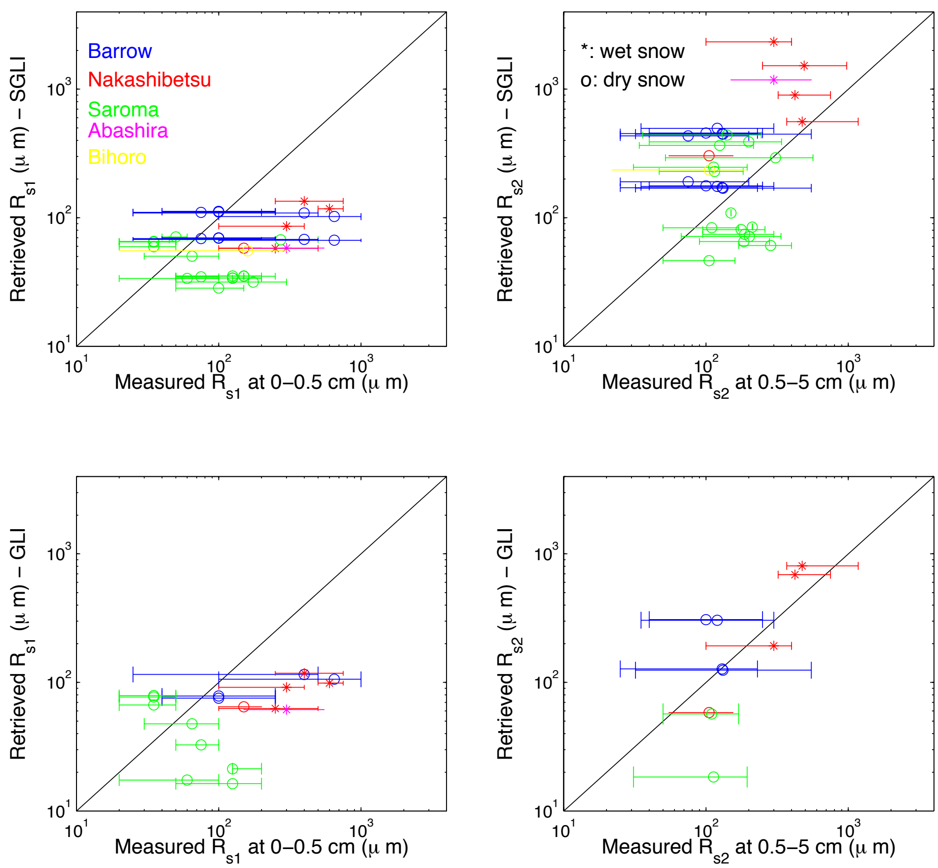

Figure 31: Snow grain sizes retrieved from the SGLI algorithm (top) and the GLI algorithm (bottom) compared with field measurements. Left: first layer grain size versus $0 - 0.5$ cm layer field measurements. Right: Second layer grain size versus $0.5 - 5$ cm layer field measurements.

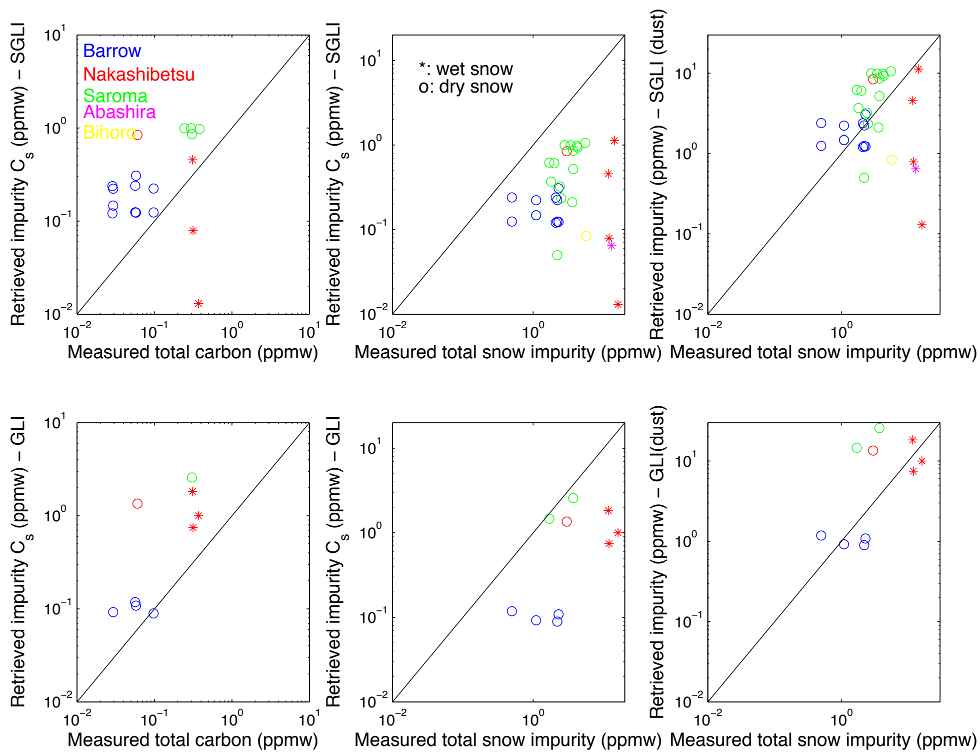

Figure 32: Snow impurity concentrations retrieved from SGLI algorithm (top) and GLI algorithm (bottom) compared with field measurements. Left: retrieved impurity versus measured total carbon. Middle: retrieved impurity versus measured total impurity. Right: equivalent dust impurity vs. measured total impurity.

Figure 32 shows the snow impurity comparison. As for the snow grain size, the SGLI results are shown in the top panels, and the GLI results in the bottom panels. In the snow model, the snow impurity concentration is assumed to be the same in both snow layers. We compare with the field measured averaged (0 - 5 cm) impurity data, and the snow impurity is assumed to consist exclusively of black carbon. In the *in-situ* snow pit work, the main composition of snow impurity was found to be mineral dust [Aoki et al., 2007a]. Since the spectral dependence of these two components are different in the visible, the results cannot be compared directly. In Fig. 32, left panels, we compare the retrieved impurity with the measured total black carbon part only, and we note that there is an overestimation of the retrieved impurity concentration. If we compare with the total measured impurity concentration which include both black carbon and mineral dust (middle panels of Fig. 32), the retrieved impurity shows an underestimation. Considering the difference between mineral dust and black carbon, and noting that mineral dust has about 10 times the effect of black carbon, we may convert the retrieved soot (black carbon) amount to an equivalent dust amount (right panels of Fig. 32), and then we get good agreement with the total measured impurity concentration. The SGLI and GLI algorithms yield similar results except that SGLI algorithm gets more retrievable pixels. We also noticed that for wet snow over Nakashibetsu,

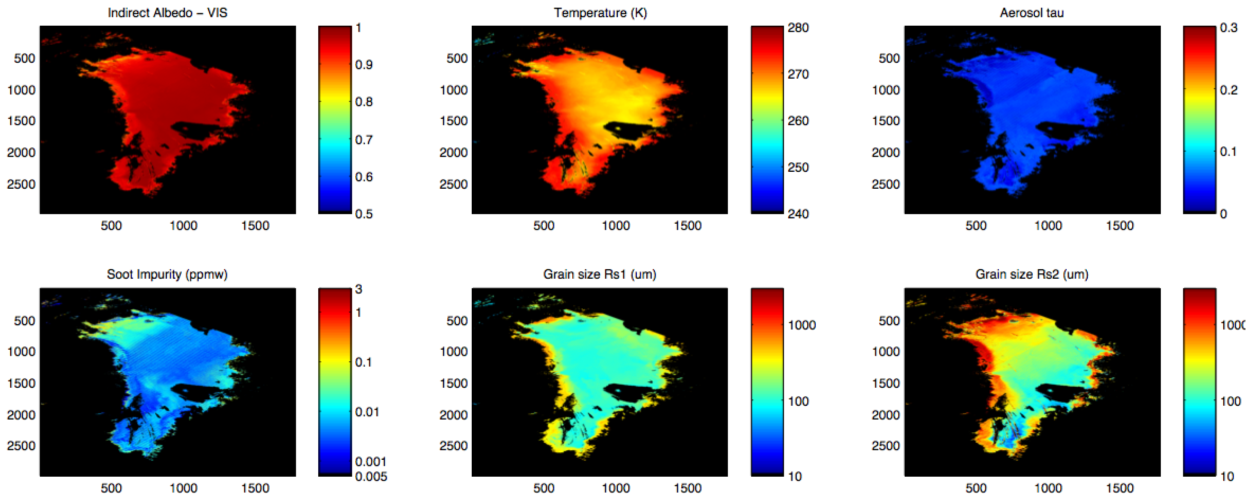

Figure 33: Snow parameter retrievals: Terra MODIS images over Greenland, Day 170, 2005.

the retrieved snow impurity is questionable too. We will test different snow impurity types and mixing conditions in our next version of the impurity retrieval algorithm, as well as the wet snow condition.

3.2.2 Application to MODIS data

We retrieved three snow physical parameters: the snow grain size in the top layer and a lower layer as well as the snow impurity concentration. MODIS data were used to test our algorithms. We found the 1.64 μm band to be sensitive to altitude and humidity, so we used the 1.24 μm band instead of the 1.64 μm band in the snow parameter retrievals. Since our retrieved snow parameters are unique and not available as standard products from MODIS or other similar sensors, a direct comparison is not possible. Availability of ground-based measurement data of snow grain sizes and impurity concentrations for validation purposes is very limited too. However, we may use the retrieved snow grain size and impurity concentrations to compute the broadband albedo, which is generally available from satellite data as well as from ground-based measurements. Because our albedo is calculated from the retrieved snow parameters, the albedo validation can be regarded as an indirect validation of the retrieved snow parameters. Figure 33 shows retrieved snow and aerosol parameters for day 170, 2005. Corresponding results derived from Aqua MODIS data are very similar and consistent with those derived from Terra MODIS data (see Fig. 38).

In year 2014, we made some improvements in the snow parameter retrieval algorithms. First, we added the elevation correction to the satellite measured radiances. This correction will improve the retrieval over high altitude areas, such as Greenland and Antarctica. Second, we changed the 1.64 μm (MODIS 1.63 μm) channels to 1.05 μm (MODIS 1.24 μm) channel for snow retrieval, because the 1.64 μm channel is too sensitive to changes in elevation and humidity. Third, this year we have greatly improved the cloud mask and surface classification algorithm. This improvement is also a big benefit to snow parameter retrievals, since cloud-contaminated pixels and sea-ice pixels will cause unreasonable snow retrievals. The quality of cloud mask and surface classification is playing a significant role in the snow/ice parameters retrieval.

In order to quantify these improvements, we re-examined a MODIS image over Greenland obtained in 2005. Using snow direct albedo, we assessed the quality of retrieved snow parameters. Figure 33 is an example for MODIS Terra data on day 170 of 2005. In Fig. 34 we compared the retrieved indirect albedo and direct albedo from 2 different versions of our algorithm. The top row shows results obtained from the version available in March 2014, and bottom row corresponding results obtained from the improved version of June 2014. The left column shows the direct albedo, the middle column shows the direct albedo, and the right column shows the absolute relative difference between the 2 albedo values. In the March 2014 version, the cloud mask had some improvements, but the surface classification was not updated yet. We can see that at the edge of the Greenland ice sheet, there are some bare ice pixels with low values of the direct albedo, not reflected in the indirect albedo, because the algorithm falsely retrieved them as "snow pixels", which led to incorrect albedo values. By June of 2014, we had upgraded the cloud mask and surface classification algorithm, and the elevation correction had also been included in snow retrieval algorithm. In this current version, the indirect albedo and the direct albedo results are very close. Hence, from this direct albedo comparison, we infer that there is a significant improvement in our snow parameter retrievals. Figure 34 is just one example. Retrievals obtained for the whole year show similar results.

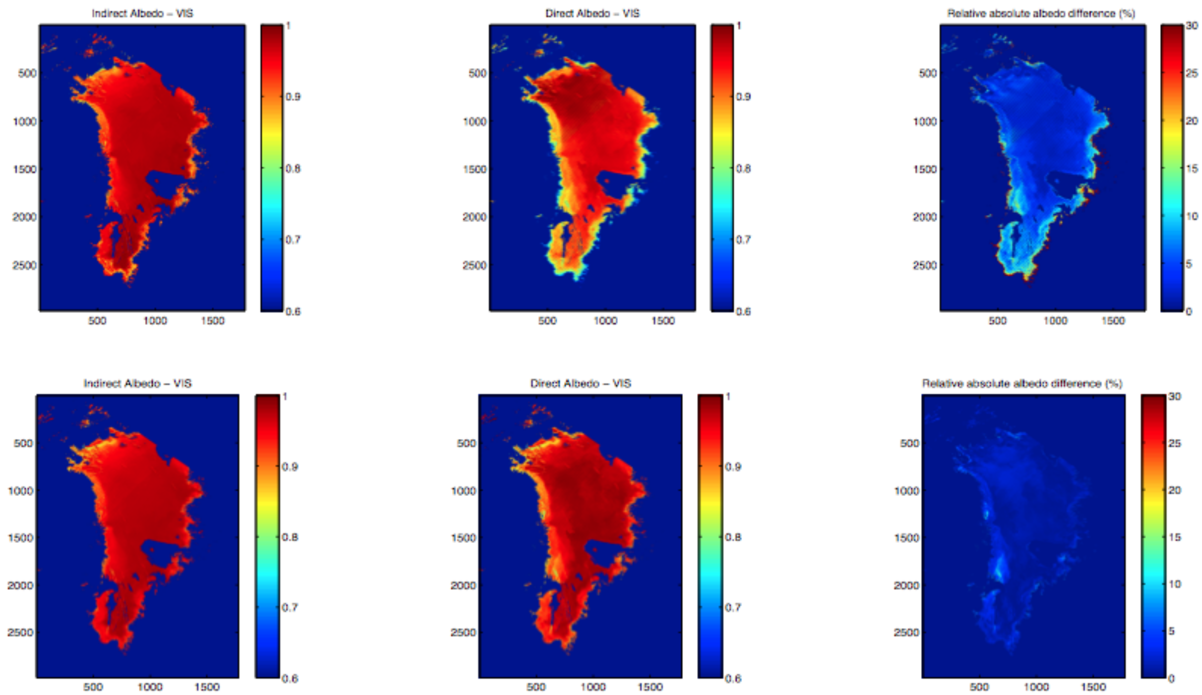

Figure 34: Snow parameter retrievals: Quality check for Terra MODIS images over Greenland, Day 170, 2005 by using different versions of cloud mask, surface classification, and snow retrieval algorithms. Top: for the version of March 2014; Bottom: for the improved version of June 2014. Left: indirect albedo; Middle: direct albedo; Right: absolute relative difference (%).

In year 2015, we updated our snow model by using the non-spherical Voronoi particle model instead of the spherical particle model. We did a comparison of modeled BRDFs with NASA aircraft CAR measurements over Barrow, Alaska in 2008 (see Fig. 14). This comparison showed that the BRDF produced by the use of a Voronoi particle model is much closer to the measured snow BRDF than the one obtained from the use of a spherical particle model. There is a significant improvement in the phase function shape of Voronoi particles, which lacks the rainbow patterns produced by a spherical particle model. In order to correctly use the Voronoi particle phase function, we used a delta-fit technique to get a smooth phase function (see section 2.2.1 and 2.4). In Figs. 35 and 36, we show 2 cases of snow retrievals, one based on a spherical snow model and the other on a non-spherical snow model. These figures clearly show the big improvement obtained from use a Voronoi particle model. The number of retrievable pixels increased by more than 20%. The image looks more smooth and the retrieved aerosol values are more reasonable.

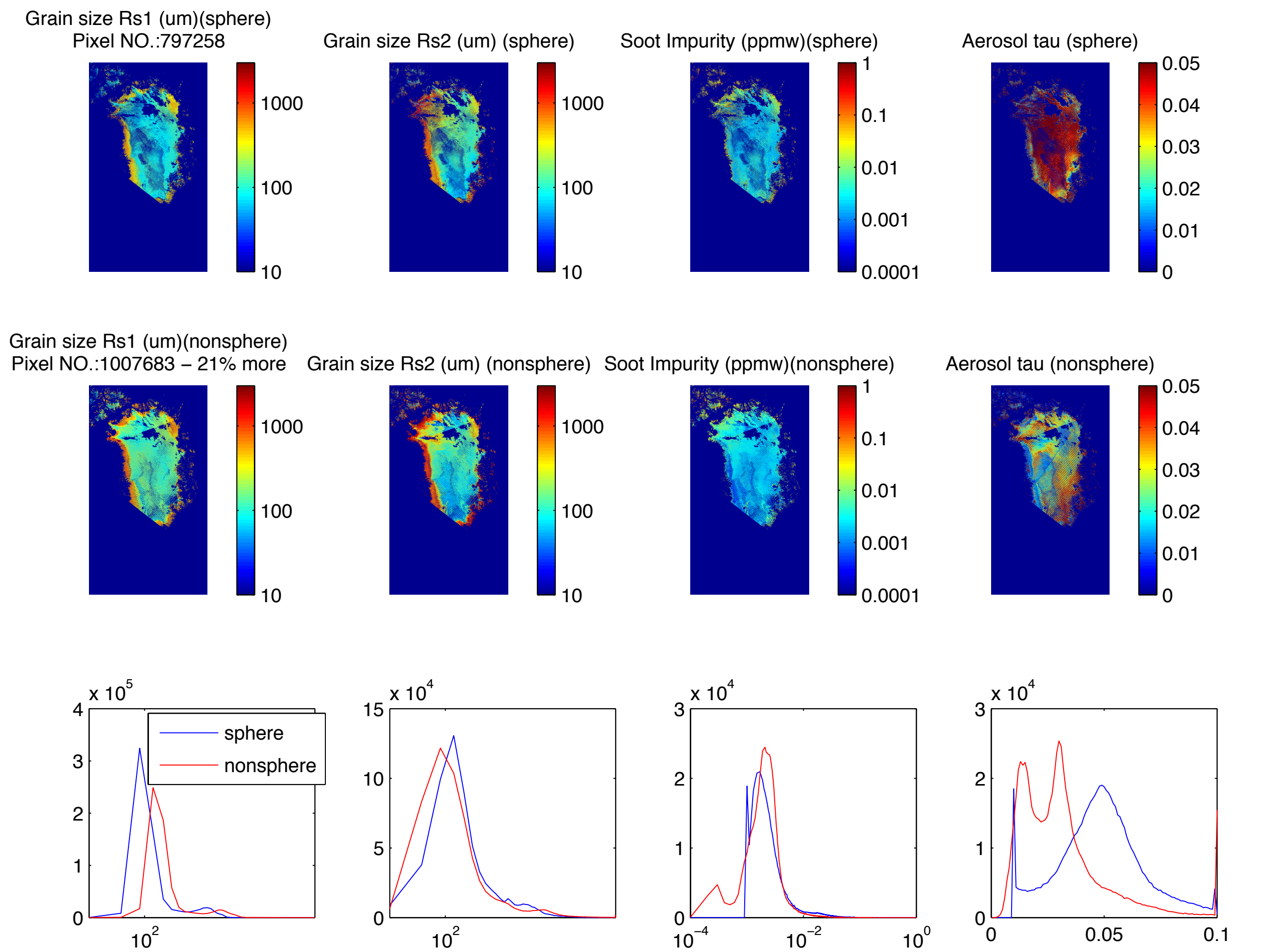

Figure 35: Snow parameter retrieval over Greenland from a spherical particle model (top panels), and from a Voronoi particle model (middle panels). The bottom row shows comparison of the retrieved number of pixels.

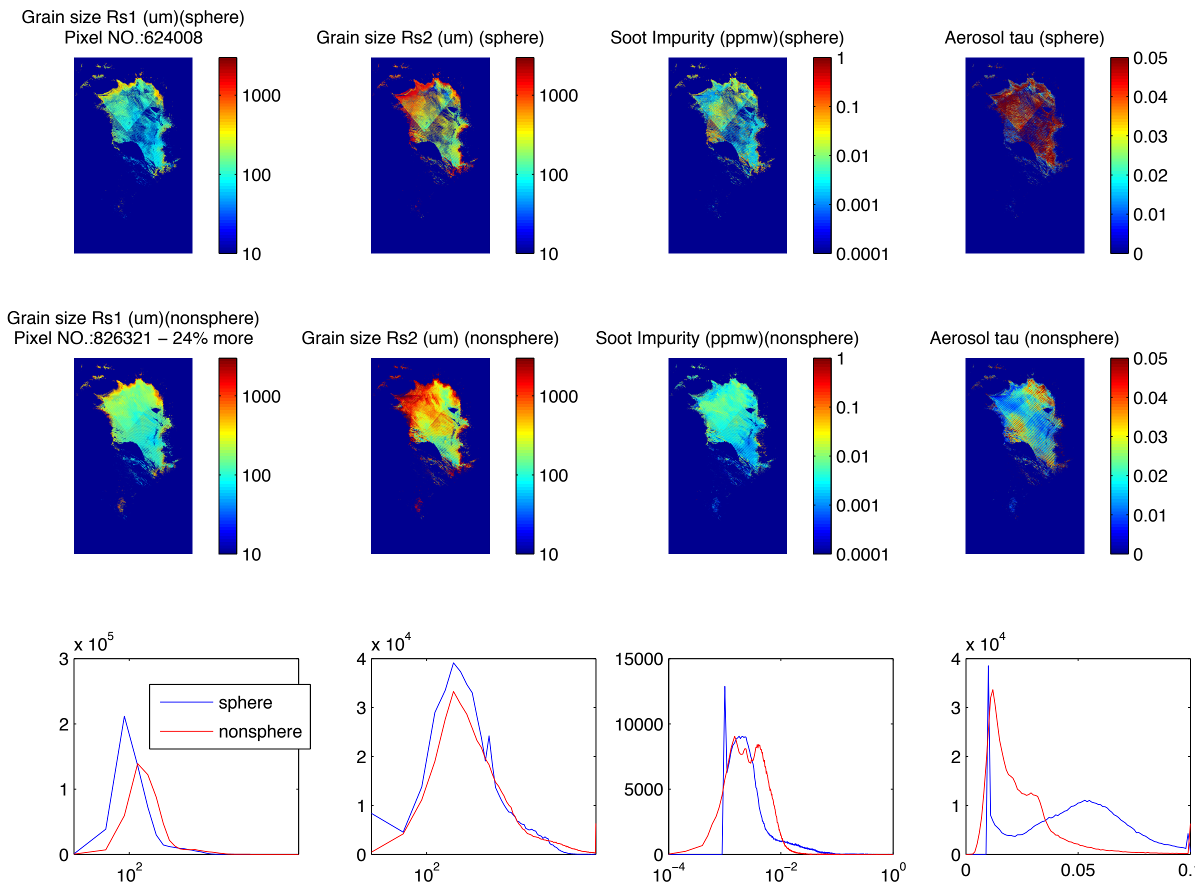

Figure 36: Saimilar retrieval as in Fig. 35 for a MODIS image over Greenland on day 191 of 2008.

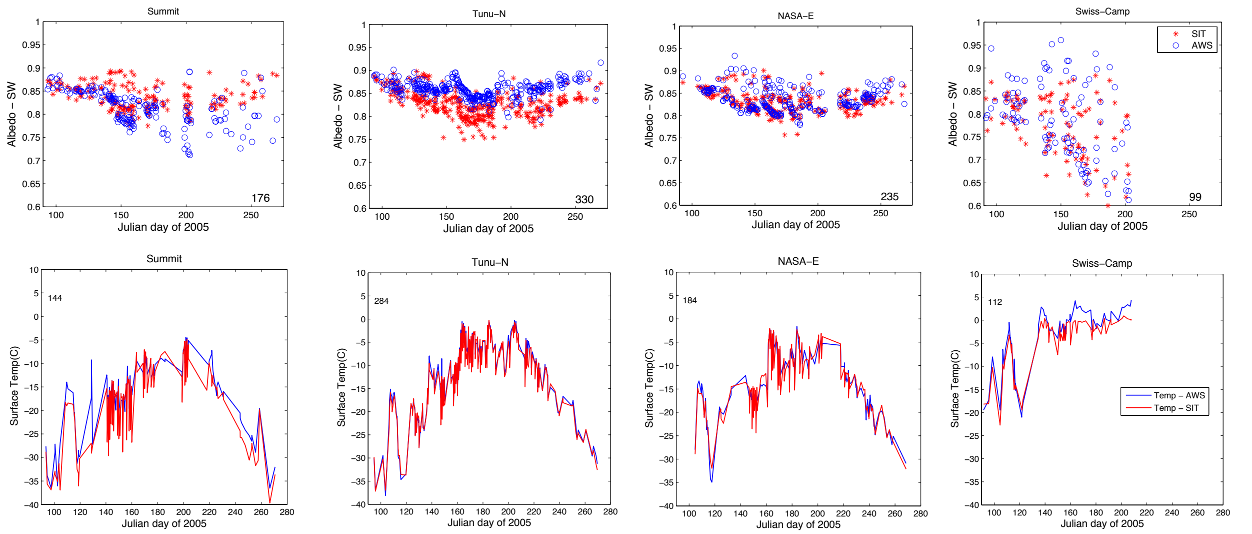

Figure 37: Snow broadband albedo and surface temperature validation against GC-NET AWS data for year 2005 in Greenland. From left to right: Summit, Tunu-N, NASA-E, Swiss-camp.

3.2.3 Snow albedo and temperature – comparisons with field measurement data

Snow/ice "particle" size and impurity concentration products are new products for EOS. One could use field measurements to validate the retrieved snow/ice "particle" size and impurity concentration [Aoki et al., 2007b], but the sparsity of field data, which may be available only for a few days of the year at a few locations, represents a significant limitation. However, field albedo measurements are relatively abundant and data sources like the Greenland Climate network (GC-NET) provide important surface measurements including air temperature, wind speed, wind direction, humidity, pressure, snow depth and albedo from 18 automatic weather stations (AWS) in Greenland. We will compare the field measured albedo with the retrieved albedo by our snow/ice albedo product. This comparison will serve as an indirect validation of our snow/ice physical parameter products such as the "particle" size and impurity concentration. Figure 37 shows some preliminary validation results with GC-NET AWS data for surface short-wave broadband albedo and temperature during year 2005. MODIS Terra data have been used by our algorithm (referred to as the SIT algorithm hereafter) to derive the surface albedo. The results show general agreement of the retrieved surface albedo and temperature with the field measurement.

Another limitation of the field measurement data is that they are obtained at one particular location and do not allow for validation of snow/ice parameter retrievals over large areas. In view of this space-time sparsity of field measurements and the critical need for validations, we propose to use the MODIS/VIIRS broadband albedo products to achieve this goal. Figure 38 shows a preliminary comparison between our albedo product with the MODIS MCD43B3 1 km albedo product using MODIS images between June 2 and 10, 2005 over Greenland. In this comparison, we configured our SIT algorithm to retrieve albedo only for snow pixels, so that land and ice pixels on the melted and melting part of Greenland are not included in our results. Figure 38 shows that there is basic agreement and we will refine it into a pixel by pixel comparison for quantitative and statistical validation.

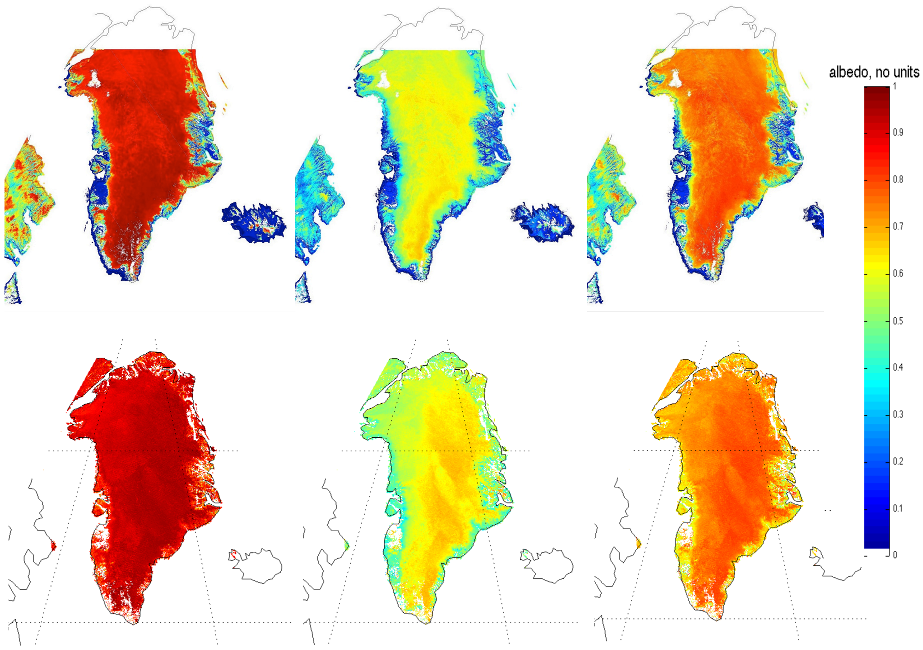

Figure 38: Albedo retrieval compared to MODIS MCD43 surface albedo between June 2 and 10, 2005 over Greenland. Upper panels: MCD43; Lower panels: SIT algorithm. From left to right: retrieved albedo for VIS (0.3-0.7 μm), NIR (0.7-2.8 μm) and SW (0.3-2.8 μm) wavelength ranges.

3.2.4 Summary

In JFY 2015, we completed the 3-year project. There were several improvements, upgrades and tests. The most important results obtained this year may be summarized as follows:

1. We acheived a very significant improvement in the cloud mask. The upgraded algorithm has been validated by use of CALIOP data, and shown to have better performance than the MODIS algorithm.

2. The surface classification algorithm has also been upgraded, especially for the sea ice/water and snow-covered sea ice/bare sea ice separation. The dynamic threshold method will also improve the accuracy of classification under different solar/viewing geometries.

3. A non-spherical Voronoi particle snow model has been implemented in the snow retrieval algorithm. A comparison of snow BRDFs obtained from model simulations and NASA CAR measurements shows that the BRDF produced by a Voronoi particle

model is closer to the measured snow BRDF than the one produced by a spherical particle model. Further, MODIS-retrieved snow parameters based on a Voronoi particle model are more accurate than those based on a spherical particle model.

4. Using response functions for the SGLI channels, we generated snow/ice surface temperature retrieval tables for the SGLI sensor, as we did for MODIS. The new tables have been implemented in the SGLI snow retrieval code.

5. We did a sensitivity study to explore the possibility of improving aerosol retrievals over snow by using the SGLI polarization channels. The results show that when the scattering angle is less than 90 degrees, the polarized reflectance could be used to distinguish effects of aerosols from those of snow impurity. The SGLI polarized sensor orbit direction design satisfy this condition. So use of polarized SGLI measuremenst could lead to improved aerosol retrievals over snow. We will continue this work in the next 3-year project.

6. In the next 3-year RA6 project, we will continue to study the non-spherical particle snow model and compare results with field measurements. Also we will explore the benefits obtained by using SGLI polarized channels and multiple angle measurements in snow retrievals. After SGLI launch, we will work on testing of the snow/ice products and further validations.

References

Ackerman, S. A., Strabala, K. I., Menzel, W. P., Frey, R. A., Moeller, C. C., & Gumley, L. E. (1998). Discriminating clear sky from clouds with MODIS. *Journal of Geophysical Research*, *103*, 32141.

Anderson, G. P., Clough, S. A., Kneizys, F. X., Chetwynd, J. H., & Shettle., E. P. (1986). *AFGL atmospheric constituent profiles (0-120km), AFGL-TR-86-0110 (OPI).* Optical Physics Division, Air Force Geophysics Laboratory Hanscom AFB, MA 01736.

Aoki, T., Aoki, T., Fukabori, M., Hachikubo, A., Tachibana, Y., & Nishio, F. (2000). Effects of snow physical parameters on spectral albedo and bi-directional reflectance of snow surface. *Journal of Geophysical Research*, *105*, 10,219 – 10,236.

Aoki, T., Hori, M., Motoyohi, H., Tanikawa, T., Hachikubo, A., Sugiura, K., Yasunari, T. J., Storvold, R., Eide, H. A., Stamnes, K., Li, W., Nieke, J., Nakajima, Y., & Takahashi, F. (2007a). ADEOS-II/GLI snow/ice products: Part II - Validation results using GLI and MODIS data. *Remote Sensing of Environment*, *111*, 274 – 290.

Aoki, T., Hori, M., Motoyoshi, H., Tanikawa, T., Hachikubo, A., Sugiura, K., Yasunari, T. J., Storvold, R., Eide, H. a., Stamnes, K., Li, W., Nieke, J., Nakajima, Y., & Takahashi, F. (2007b). ADEOS-II/GLI snow/ice products Part II: Validation results using GLI and MODIS data. *Remote Sensing of Environment*, *111*, 274–290.

Barton, I. J. (1985). Transmission model and ground-truth investigation of satellite-derived sea surface temperatures. *J. Clim. Appl. Meteorol.*, *24*, 508 – 516.

Blanchet, J. P., & List, R. (1983). Estimation of optical properties of arctic haze using a numerical model. *Atmos. Ocean.*, *21*, 444–465.

Chen, N., Li, W., Tanikawa, T., Hori, M., Aoki, T., & Stamnes, K. (2014). Cloud Mask Over Snow/ice Covered Areas for the GCOM-C1/SGLI Cryosphere Mission: Validations over Greenland. *Journal of Geophysical Research: Atmospheres*, *119*.

Dahlback, A., & Stamnes, K. (1991). A new spherical model for computing the radiation field available for photolysis and heating at twilight. *Planetary and Space Science*, *39*, 671–683.

Dozier, J., & Warren, S. G. (1982). Effect of viewing angle on the infrared brightness temperature of snow. *Water Resour. Res.*, *18*, 1424–1434.

Ettema, J., van den Broeke, M. R., van Meijgaard, E., van de Berg, W. J., Box, J. E., & Steffen, K. (2010). Climate of the Greenland ice sheet using a high-resolution climate model – Part 1: Evaluation. *The Cryosphere*, *4*, 511–527.

Gjerstad, K. I., Stamnes, J. J., Hamre, B., Lotsberg, J. K., Yan, B., & Stamnes, K. (2003). Monte carlo and discrete-ordinate simulations of irradiances in the coupled atmosphere-ocean system. *Applied Optics*, *42*, 2609 – 2622.

Grenfell, T. C., & Warren, S. G. (1999a). Relationship of a nonspherical ice particle by a collection of independent sphere for scattering and absorption of radiation. *Journal of Geophysical Research*, *104*, 31,697 – 31,709.

Grenfell, T. C., & Warren, S. G. (1999b). Representation of a nonspherical ice particle by a collection of independent sphere for scattering and absorption of radiation. *Journal of Geophysical Research*, *104*, 31697–31709.

Hall, D. K., Box, J. E., Casey, K. A., Hook, S. J., Shuman, C. A., & Steffen, K. (2008). Comparison of satellite-derived and in-situ observations of ice and snow surface temperatures over greenland. *Remote Sensing of Environment*, *112*, 3739–3749.

Hall, D. K., Riggs, G. A., & Barton, J. S. (2001). *Algorithm Theoretical Basis Document (ATBD) for the MODIS Snow and Sea Ice-Mapping Algorithms*. Technical Report September.

Hall, D. K., Riggs, G. A., & Salomonson, V. V. (1995). Development of Methods for Mapping Global Snow Cover Using Moderate Resolution Imaging Spectroradiometer Data. *Remote Sensing of Environment*, *34*, 127–140.

Hall, D. K., Riggs, G. A., & Salomonson, V. V. (1996). *Algorithm Theoretical Basis Document (ATBD) for the MODIS Snow and Sea Ice-Mapping Algorithms*. Technical Report September.

Hamre, B., Winther, J.-G., Gerland, S., Stamnes, J. J., & Stamnes, K. (2004). Modeled and measured optical transmittance of snow-covered first-year sea ice in kongsfjorden, svalbard. *Journal of Geophysical Research: Oceans*, *109*.

Hanssen, A., & Kuipers, W. (1965). *On the Relationship Between the Frequency of Rain and Various Meteorological Parameters: (with Reference to the Problem Ob Objective Forecasting)*. Mededelingen en verhandelingen. Staatsdrukkerij- en Uitgeverijbedrijf.

Hess, M., Koepke, P., & Schult, I. (1998). Optical properties of aerosols and clouds: The software package opac. *Bulletin of the American Meteorological Society*, *79*, 831 – 844.

Holz, R. E., Ackerman, S. A., Nagle, F. W., Frey, R., Dutcher, S., Kuehn, R. E., Vaughan, M. A., & Baum, B. (2008). Global Moderate Resolution Imaging Spectroradiometer (MODIS) cloud detection and height evaluation using CALIOP. *Journal of Geophysical Research*, *113*, D00A19.

Hori, M., Aoki, T., Tanikawa, T., Motoyoshi, H., Hachikubo, A., Suqiura, K., T J Yasunari, H. E., Storvold, R., Nakajima, Y., & Takahashi, F. (2006). In-situ measured spectral directional emissivity of snow and ice in the 8?14 μm atmospheric window. *Remote Sensing of Environment*, *100*, 486?502.

Hu, Y. X., & Stamnes, K. (1993). An Accurate Parameterization of the Radiative Properties of Water Clouds Suitable for Use in Climate Models. *Journal of Climate*, *6*, 728–742.

Hutchison, K. D., Iisager, B. D., & Mahoney, R. L. (2013). Enhanced snow and ice identification with the VIIRS cloud mask algorithm. *Remote Sensing Letters*, *4*, 929–936.

Jiang, S., Stamnes, K., Li, W., & Hamre, B. (2005). Enhanced solar irradiance across the atmosphere–sea ice interface: a quantitative numerical study. *Appl. Opt.*, *44*, 2613–2625.

Jin, Z., Stamnes, K., Weeks, W. F., & Tsay, S.-C. (1994). The effect of sea ice on the solar energy budget in the atmosphere-sea ice-ocean system: A model study. *Journal of Geophysical Research: Oceans*, *99*, 25281–25294.

Key, J. R., Collins, J. B., Fowler, C., & Stone, R. S. (1997). High-latitude surface temperature estimates from thermal satellite data. *Remote Sens. Environ.*, *67*, 302 – 309.

Key, J. R., & Haefliger, M. (1992). Tba. *J. Geophys. Res.*, *67*, 5885 – 5893.

Key, J. R., Yang, P., Baum, B. A., & Nasiri, S. L. (2002). Parameterization of shortwave ice cloud optical properties for various particle habits. *Journal of Geophysical Research*, *107*, 1–10.

Kuchiki, K., Aoki, T., Niwano, M., Motoyoshi, H., & Iwabuchi, H. (2011). Effect of sastrugi on snow bidirectional reflectance and its application to MODIS data. *Journal of Geophysical Research*, *116*, D18110.

Li, W., Stamnes, K., Eide, H., & Spurr, R. (2007). Bidirectional reflectance distribution function of snow: corrections for the lambertian assumption in remote sensing applications. *Optical Engineering*, *46*, 066201–066201–9.

Li, W., Stamnes, K., Spurr, R., & Stamnes, J. (2008). Simultaneous retrieval of aerosol and ocean properties by optimal estimation: Seawifs case studies for the santa barbara channel. *International Journal of Remote Sensing*, *29*, 5689 – 5698.

Liu, Y., Ackerman, S. A., Maddux, B. C., Key, J. R., & Frey, R. A. (2010). Errors in Cloud Detection over the Arctic Using a Satellite Imager and Implications for Observing Feedback Mechanisms. *Journal of Climate*, *23*, 1894–1907.

Llewellyn-Jones, D. T., Minnett, P. J., Saunders, R. W., & Zavody, A. M. (1984). Satellite multichannel infrared measurements of sea surface temperature of the northeast atlantic ocean using avhrr/2. *Q. J. R. Meteorol. Soc.*, *110*, 613 – 631.

McClain, E. P., Pichel, W. G., & Walton, C. C. (1985). Comparative performance of avhrr-based multichannel sea surface temperature. *J. Geophys. Res.*, *18*, 11587–11601.

Miller, S. D., & Lee, T. F. (2005). Satellite-Based Imagery Techniques for Daytime Cloud / Snow Delineation from MODIS. *Journal of Applied Meteorology*, *44*, 987–997.

Minnett, P. J. (1990). The regional optimization of infrared measurements of sea surface temperature from space. *J. Geophys. Res.*, *95*, 13497 – 13510.

Price, J. C. (1983). Estimating surface temperature from satellite thermal infrared data – a simple formulation for the atmospheric effect. *Remote Sens. of Environ.*, *13*, 353–361.

Rodgers, C. D. (2000). *Inverse methods for atmospheric sounding - Theory and Practice -*. Series on Atmospheric, Oceanic and Planetary Physics. World Scientific.

Salomonson, V., & Appel, I. (2004). Estimating fractional snow cover from MODIS using the normalized difference snow index. *Remote Sensing of Environment*, *89*, 351–360.

Salomonson, V., & Appel, I. (2006). Development of the Aqua MODIS NDSI fractional snow cover algorithm and validation results. *IEEE Transactions on Geoscience and Remote Sensing*, *44*, 1747–1756.

Spurr, R. (2002). Simultaneous derivation of intensities and weighting functions in a general pseudo-spherical discrete ordinate radiative transfer treatment. *Journal of Quantitative Spectroscopy and Radiative Transfer*, *75*, 129 – 175.

Stamnes, K., Hamre, B., Stamnes, J., Ryzhikov, G., Biryulina, M., Mahoney, R., Hauss, B., & Sei, a. (2011). Modeling of radiation transport in coupled atmosphere-snow-ice-ocean systems. *Journal of Quantitative Spectroscopy and Radiative Transfer*, *112*, 714–726.

Stamnes, K., Li, W., Eide, H., Aoki, T., Hori, M., & Storvold, R. (2007a). ADEOS-II/GLI snow/ice products Part I: Scientific basis. *Remote Sensing of Environment*, *111*, 258–273.

Stamnes, K., Tsay, S. C., Wiscombe, W., & Jayaweera, K. (1988a). Numerically stable algorithm for discrete-ordinate-method radiative transfer in multiple scattering and emitting layered media. *Applied optics*, *27*, 2502–9.

Stamnes, K., Tsay, S. C., Wiscombe, W. J., & Jayaweera, K. (1988b). Numerically stable algorithm for discrete-ordinate-method radiative transfer in multiple scattering and emitting layered media. *Applied Optics*, *27*, 2502 – 2509.

Stamnes, K., Wei, L., Eide, H., Aoki, T., Hori, M., & Storvold, R. (2007b). ADEOS-II/GLI snow/ice products: Part I - Scientific basis. *Remote Sensing of Environment*, *111*, 258 – 273.

Trepte, Q., Minnis, P., & Arduini, R. F. (2002). Daytime and nighttime polar cloud and snow identification using MODIS data. In *Proc. SPIE 3rd International Asia-Pacific Environmental Remote Sensing Symposium: Remote Sensing of the Atmosphere, Ocean, Environment, and Space, Hangzhou, China, October 23-27* (pp. 449–459).

Wan, Z. (2008). New refinements and validation of the modis land-surface temperature/emissivity products. *Remote Sensing of Environment*, *112*, 59?74.

Wan, Z., & Dozier, J. (1996). A generalized split-window algorithm for retrieving land-surface temperature from space. *IEEE Trans. Geosci. Remote Sens.*, *34*, 892–905.

Warren, S. G. (1982). Optical properties of snow. *Reviews of Geophysics and Space Physics*, *20*, 67 – 89.

Warren, S. G., & Brandt, R. E. (2008). Optical constants of ice from the ultraviolet to the microwave: A revised compilation. *Journal of Geophysical Research*, *113*, D14220. doi:10.1029/2007JD009744.

Warren, S. G., Brandt, R. E., & Hinton, P. O. (1998). Effect of surface roughness on bidirectional reflectance of Antarctic snow. *Journal of Geophysical Research*, *103*, 25789–25807.